

A new nonreactive force field for accurate molecular dynamics simulations of TATB at extreme conditions

Matthew P. Kroonblawd,^{*,†} Paul Lafourcade,^{*,‡,§} Laurence E. Fried,[†]

Jean-Bernard Maillet,^{‡,§} and Tommy Sewell[¶]

[†]*Physical and Life Sciences Directorate, Lawrence Livermore National Laboratory,
Livermore, CA 94550, United States*

[‡]*CEA DAM DIF, F-91297 Arpajon, France*

[¶]*Department of Chemistry, University of Missouri, Columbia, Missouri 65211, United
States;*

[§]*Université Paris-Saclay, LMCE, F-91689 Bruyères-le-Châtel, France*

E-mail: kroonblawd1@llnl.gov; paul.lafourcade@cea.fr

Abstract

Insensitive high explosives based on TATB (1,3,5-triamino-2,4,6-trinitrobenzene) are needed in applications when safety is of paramount importance, but the basic material properties that give rise to its insensitivity are not fully understood. Molecular dynamics (MD) modeling using empirical force fields (FFs) has been the main route to characterize many complicated dynamical properties of the single crystal, but these FFs have not been comprehensively tested at extreme conditions typical of detonation. We collect a benchmark data set of (quasi)static TATB physical properties as determined by experiments and electronic structure calculations and apply this data set to validate four existing TATB FFs along with a new TATB FF that we develop here and denote as the CEA-LLNL-Missouri (CLM) FF. Benchmark data include vibrational spectra, the TATB crystal temperature-pressure-dependent equation of state and lattice parameters, properties of TATB crystal polymorphs and transitions to the gaseous and liquid states, dimer energy landscapes, the pressure-dependent elastic tensor, and the energy landscape for inelastic deformation via sliding of TATB crystal layers. As a general assessment, we find that the existing nonreactive FFs are more accurate in describing TATB's physical properties than the ReaxFF-based variants. The new CLM FF is found to consistently yield similar or better agreement with experiments and electronic structure theory than any of the existing FF models, and it presents a distinct improvement in accurately modeling TATB elasticity and equation of state. This work is expected to help improve the accuracy of FF-based modeling of complicated dynamic responses that ultimately govern the safety and performance characteristics of this material.

1 Introduction

Insensitive high explosives (IHEs) based on the energetic molecule 1,3,5-triamino-2,4,6-trinitrobenzene (TATB) are almost unique in their safety-performance trade-offs. TATB is a layered crystalline material comprised of 2D hydrogen-bonded sheets that stack in a

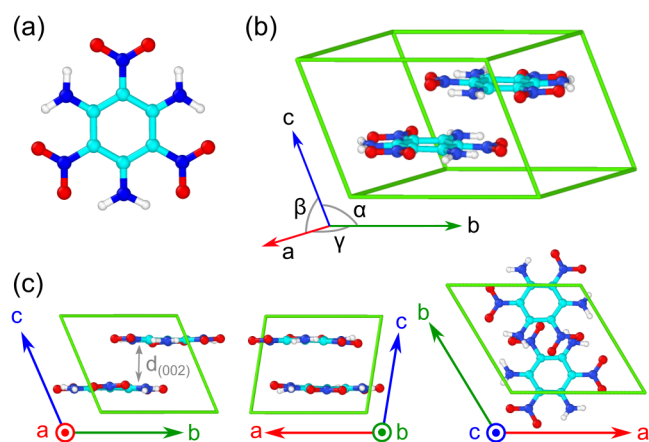


Figure 1: The structure of (a) the TATB molecule, (b) the triclinic $P\bar{1}$ TATB primitive unit cell, and (c) selected projections of the $P\bar{1}$ unit cell along lattice vectors \mathbf{a} , \mathbf{b} , and \mathbf{c} .

graphitic-like motif (see Figure 1).¹ In a history of TATB current to 1994, Dobratz² placed the earliest recorded synthesis of TATB to the 1888 report of Jackson and Wing.³ Although TATB was not at first recognized as an explosive, it has gained significant traction since the 1950s for use as an HE with highly desirable safety characteristics. Rice and Simpson noted in 1990 that TATB is a “reasonably powerful high explosive whose thermal and shock stability is considerably greater than that of any other known material of comparable energy.” While more recently synthesized energetic molecules such as 1,1-diamino-2,2-dinitroethylene (FOX-7)⁴ and 2,6-diamino-3,5-dinitropyrazine-1-oxide (LLM-105)⁵ show promise as potential IHEs, there is currently no accepted alternative to TATB for applications with stringent safety requirements. The origins of TATB’s unusual safety characteristics have been the subject of conjecture for decades and remain open to debate,⁶ but the prospect of rapidly synthesizing new IHEs⁷ provides strong motivation for developing a scientific understanding of how TATB’s material properties give rise to its insensitivity.

Many properties of TATB crystal remain poorly constrained by experimental measurements, especially at the high temperatures and pressures typical of HE initiation and detonation. (For reference, TATB has a von Neumann shock pressure of ≈ 34 GPa⁸ and its decomposition products can reach upwards of 4000 K.⁹) As will be elaborated below, this has left molecular modeling techniques using either electronic structure methods or empiri-

cal force fields (FFs) as the only practical route to obtain many TATB material properties. Molecular dynamics (MD) simulations using empirical FFs have been instrumental in characterizing anisotropic properties of TATB single crystals as functions of temperature and pressure. Despite this utility, the two main nonreactive FFs developed for TATB (by Gee et al.¹⁰ and Bedrov et al.¹¹) were originally parameterized in the mid-to-late 2000s and the two most widely used ReaxFF-based FFs applied to HEs (namely the ReaxFF-LG¹² and ReaxFF-2018¹³ variants) have not been specifically trained for TATB. A small but growing body of experimental work is now available to directly test the predictive accuracy of these FFs in extrapolating to higher pressures. Preliminary comparisons^{14,15} against the high-pressure equation of state (EOS) measurements by Plisson et al.¹⁶ indicate that a new revised TATB FF is needed to more accurately model the crystal under detonation conditions.

To this end, we have collected from the literature what is intended to be a comprehensive set of physical properties of TATB crystal to be used as benchmarks for testing legacy and new FFs for TATB. Where possible, priority is given to comparisons against experimental measurements. However, some vital information (e.g., the elastic tensor) needed for accurately modeling TATB crystal mechanics has only been constrained using electronic structure methods such as density functional theory (DFT) and the FFs themselves. In what follows, we first summarize the set of TATB crystal physical properties that have been determined through experiments or electronic structure calculations. We then identify those physical properties which have only been determined using empirical FFs, both to highlight the range of properties that remain “loosely” constrained and to emphasize the need for well-validated FFs. These data serve as a basis for comprehensive validation testing of widely used TATB FFs and for a newly developed nonreactive FF that we propose here, which we denote by our respective institutions as the CEA-LLNL-Missouri FF (or CLM FF).

Among the most tightly constrained physical properties of TATB crystal is the EOS and lattice parameters of the triclinic crystal polymorph first identified by Cady and Larson¹ in 1965. Diamond anvil cell experiments have been applied to characterize the isothermal

pressure-volume (PV) response and lattice parameters at room temperature. Two notable sets of data include the 2008 measurements by Stevens et al.,¹⁷ which went up to 13 GPa, and more recently the 2017 experiments by Plisson et al.,¹⁶ which reach up to 66 GPa. Isobaric temperature-volume (TV) responses and lattice parameters have also been determined at atmospheric pressure, along with the derived thermal expansion coefficients. The 1979 report by Kolb and Rizzo¹⁸ considered temperatures as low as 212 K whereas the 2010 report by Sun et al.¹⁹ probed temperatures as high as 511 K. The above EOS studies have revealed considerable mechanical anisotropy in TATB crystal, which exhibits significantly greater compressibility and coefficient of thermal expansion for the direction normal to the 2D crystal layers compared to directions within the layers.

Compared to the above static mechanical responses, dynamic properties of the single crystal involving mechanical strength are much less well characterized by experiments. The recent 2020 report on oriented shocks in TATB single crystal by Marshall et al.²⁰ provides constraints on accessible Hugoniot states, albeit for only a single direction: compression normal to the TATB crystal layers. Taw et al.²¹ probed the hardness and yield strength of the (001) facet through nanoindentation experiments (indenting normal to the crystal layers); these two properties were found to be at least qualitatively consistent with earlier MD predictions.²² Timescales for these dynamic experiments are considerably longer than typical MD simulations, and at the same time it is understood that processes involving inelastic deformations can exhibit strong kinetic effects and sensitivity to initial microstructural defects.²³⁻²⁵ Thus, while there is limited experimental data available on TATB single crystal strength, forming direct one-to-one comparisons against MD must be handled with careful consideration.

Transformations from the solid triclinic polymorph have been explored in experiments. The studies by Rosen and Dickinson²⁶ and by Garza²⁷ have characterized the enthalpy of sublimation, which is a measure of crystal binding energy and is directly connected to the accuracy of specific FF potential energy function terms. While TATB is a non-melt-

castable explosive, the melting point has been estimated at atmospheric pressure by both Stolovey et al.²⁸ in 1983 and Bowlan et al.²⁹ in 2022, with both reports yielding values near 700 K. Polymorphism in TATB has been the subject of speculation for decades, with several reports^{18,30} proposing alternative crystal structures that exhibit similar layered motifs to the Cady and Larson structure. While these transitions have not been verified, a recent 2019 single-crystal diffraction study by Steele et al.³¹ identified a high-pressure monoclinic polymorph above ≈ 4 GPa along with the lattice parameters of the monoclinic phase up to 16 GPa. The monoclinic and triclinic packing structures were found to be very similar and electronic structure calculations indicated that the two structures were essentially isenthalpic, although the free energy landscape for this transition remains unquantified.

Detailed spectroscopic studies have characterized the vibrational density of states of TATB crystal. The available reports span several different spectroscopic techniques, including inelastic neutron scattering,³² Raman,^{33,34} and IR³⁵ measurements. This kind of data directly probes the high-dimensional potential energy surface governing intramolecular motions and therefore provides very strong constraints on specific FF terms.

A somewhat more narrow list of TATB properties have only been determined using electronic structure techniques. The most important of these are arguably the elastic tensor coefficients C_{ij} , which have been characterized within the harmonic approximation as a function of pressure at 0 K. Valenzano et al.³⁶ obtained a subset of the C_{ij} at a single volume state using hybrid DFT whereas Rykounov³⁷ and Qin et al.³⁸ used more efficient generalized gradient approximation DFT functionals to characterize the full C_{ij} at pressures reaching 10 GPa and 30 GPa, respectively. Long and Chen³⁹ used DFT calculations to predict the anisotropic thermal conductivity of TATB crystal under approximations that only considered two-phonon processes. Properties that are less directly observable in experiments have also been characterized, including TATB dimer interaction energies by Taylor⁴⁰ and the energy landscape for a specific deformation mechanism involving glide of crystal layers by Zhang and coworkers.^{41,42}

Many properties of TATB crystal remain determined only through application of empirical FFs. These include the pressure-temperature dependent elastic coefficients $C_{ij}(P, T)$, which have been probed using variants of both the Bedrov FF^{11,15} and the Gee FF.⁴³ Inelastic deformation modes and anisotropic strength properties of TATB single crystal have almost exclusively been studied through MD simulations with variants of the Bedrov FF.^{14,44-49} Melting behavior, including anisotropic surface melting⁵⁰ and the pressure-dependent melt curve,⁵¹ serve as important physics governing material strength, but have only been assessed using the Bedrov FF. Assessments of the pressure-temperature dependent anisotropic thermal conductivity have been made using variants of the Bedrov FF⁵²⁻⁵⁴ and Gee FF.⁴³ Shock responses along general directions in the crystal have only been determined with MD,⁴⁹ as have the anisotropic mechanics of hot spot formation⁵⁵⁻⁵⁸ and thermal relaxation^{59,60} processes. All of these FF-derived material properties, including their functional dependencies, are essential components for⁶¹ (and/or validation tests of) continuum-based multiphysics simulations that are increasingly used to predict HE initiation behavior (see, for example Ref. 55).

The remainder of this article is organized as follows. In Section 2 we briefly summarize MD calculation details and outline a set of three nonreactive and two reactive FFs for TATB, including our new nonreactive CLM FF. In Section 3, the accuracy of these FFs is then assessed against literature reports on a wide range of (quasi)static TATB physical properties as determined by experiment or electronic structure calculations. These include properties closely coupled the accuracy of inter- and intramolecular FF potential energy functions in Section 3.1, the EOS of the triclinic phase in Section 3.2, transformations to other phases in Section 3.3, the pressure-dependent elastic coefficients in Section 3.4, and the mechanics of layer sliding in Section 3.5. Comparisons to complicated dynamic material properties such as strength and the shock response above the Hugoniot elastic limit are the subject of ongoing work. Conclusions and a prospectus for future TATB FF development are drawn in Section 4.

2 Methods

2.1 Classical MD Simulation Details

All classical MD simulations were performed using the LAMMPS MD code,⁶² 3D periodic simulation cells, and FFs which are described in detail below. Isothermal-isochoric (*NVT*) and isothermal-isobaric (*NPT*) simulations were performed at various points throughout this study using a Nosé-Hoover-style thermostat and barostat.^{63,64} The thermostat time constant was set to 100 fs and the barostat time constant was set to 1 ps and included the optional drag term, which was set to 1.0 (unitless). All six independent stress components were coupled to respective independent barostats in simulations involving TATB crystal under *NPT* conditions. Unless otherwise noted, all trajectories with nonreactive FFs were integrated with a 0.5 fs timestep and trajectories with reactive FFs were integrated with a 0.1 fs timestep. Optimizations of the TATB molecule and crystal at 0 K were performed using minimum relative energy and force tolerances of 10^{-8} . Details concerning the calculation of specific TATB physical properties all used well-established methods and are described briefly at relevant points in the Results and Discussion (Section 3) and Supporting Information.

2.2 Nonreactive Force Fields

2.2.1 General Details

Three nonreactive classical FFs were considered that were specifically developed for TATB. These include a widely used variant of the well-established FF by Bedrov et al.,¹¹ a revised version of the FF by Gee et al.,¹⁰ and a new FF that we developed here denoted as the CEA-LLNL-Missouri FF (CLM FF). All three FFs adopt a similar Class-I function form

$$U_{\text{tot}} = \sum_{\text{bonds}} U_{\text{bnd}} + \sum_{\text{angles}} U_{\text{ang}} + \sum_{\text{dihedrals}} U_{\text{dih}} + \sum_{\text{impropers}} U_{\text{imp}} + \sum_{\text{intraOHpairs}} U_{\text{OH}} + \sum_{\text{pairs}} U_{\text{NB}}, \quad (1)$$

in which the total potential energy (U_{tot}) is expressed as a sum over two-center bonds (U_{bnd}), three-center angles (U_{ang}), four-center proper and improper dihedrals (U_{dih} and U_{imp}), a repulsive potential that is defined between the O and H atoms within a given molecule (U_{OH}), and nonbonded pairwise interactions (U_{NB}) that include repulsion-dispersion terms and Coulombic electrostatics between fixed partial charges that are located on the nuclei. All three FFs adopt non-standard conventions for exclusion of intramolecular pairwise interactions, which are discussed in detail for each FF below. Nonbonded pairwise interactions were evaluated in real space up to an 11 Å cutoff and electrostatic interactions were computed in real space using the linear-scaling Wolf potential⁶⁵ with the damping term set to 0.2 Å and an 11 Å cutoff.

Covalent terms in these three FFs adopted similar functional forms and in some cases the same parameters. All bonds and angles are modeled as harmonic functions and proper dihedrals are modeled using truncated cosine series. The Bedrov and CLM FFs both include improper dihedrals modeled as harmonic functions whereas the Revised Gee FF does not include any improper dihedrals. All three FFs use the same intramolecular OH repulsion term

$$U_{\text{OH}}(r) = A \cdot \exp\left(-\frac{r}{B}\right), \quad (2)$$

where $A = 15935 \text{ kcal}\cdot\text{mol}^{-1}$ and $B = 0.1453 \text{ Å}$. This repulsive OH term was originally developed in Ref. 50 for the Bedrov FF to prevent unphysically close atomic contacts in the liquid phase that can arise due to intramolecular nonbonded pairwise exclusions. We implemented U_{OH} as a tabulated bond, which has consequences for the intramolecular nonbonded exclusions (discussed below). Example LAMMPS input files for all three FFs are provided in the Supporting Information.

2.2.2 Bedrov FF

The most widely used version of the Bedrov FF, and the one we consider here, stems from the original non-polarizable version originally proposed in the 2009 report by Bedrov et

al.¹¹ The original FF version treated all two-center bond vibrations as rigid and excluded all intramolecular nonbonded interactions. The latter choice was made due to TATB’s molecular structure, which is approximately planar and leads to close 1-6 interactions between the nitro and amine groups. These close contacts lead to difficulties in parameterizing flexible FFs not encountered in rigid-molecule FF models such as the TraPPE FF⁶⁶ and the TATB FF by Taylor.⁴⁰ Contributions from these contacts to the total energy (as predicted by electronic structure calculations) were instead built into the dihedral potentials. Similar choices were made in the parameterization of the flexible Gee FF.

Intermolecular repulsion and dispersion interactions in the Bedrov FF are modeled using a hybrid of the Buckingham and Lennard-Jones functional forms (exp-6-12), with the total nonbonded potential energy being

$$U_{\text{NB}}^{\text{Bedrov}}(r) = \sum_{\text{pairs}} A_{\alpha\beta} \cdot \exp(-B_{\alpha\beta} \cdot r) - C_{\alpha\beta} \cdot r^{-6} + D \left(\frac{12}{B_{\alpha\beta} \cdot r} \right)^{12} + \frac{q_{\alpha}q_{\beta}}{4\pi\epsilon_0 r}. \quad (3)$$

Here, α and β denote specific atom types with heteroatom pair interaction coefficients ($A_{\alpha\beta}$, $B_{\alpha\beta}$, and $C_{\alpha\beta}$) determined using Waldman-Hagler mixing rules,⁶⁷ the q are partial electric charges, and ϵ_0 is the dielectric permittivity of vacuum. The extra r^{-12} term in Eq. 3 compensates for the divergence in the standard exp-6 form at small separations, with $D = 5 \times 10^{-5}$ kcal·mol⁻¹ for all pair types. A hybrid overlay is used to implement the separate terms of this function in LAMMPS as described in Ref. 55.

In 2013, Kroonblawd and Sewell⁵² proposed a fully flexible version of the Bedrov FF that included harmonic U_{bnd} and U_{ang} terms that were specifically tuned to reproduce experimental TATB vibrational Raman spectra³³ and DFT predictions for the normal mode frequencies and eigenvector assignments.⁶⁸ Later application of the fully flexible Bedrov FF to TATB liquid by Mathew et al.⁵⁰ in 2015 revealed that the exclusion of all intramolecular nonbonded terms resulted in unphysically close contacts between the nitro and amine groups. To compensate for this, those authors developed Eq. 2 based on DFT calculations.

We note that Eq. 2 is defined for every distinct O-H pair within a molecule as a tabulated bond potential, leading to an “extra” 36 FF topological bond definitions per molecule beyond the 24 “real” covalent bonds. Essentially all subsequent applications of the Bedrov FF have included both the bond/angle terms by Kroonblawd and Sewell and the intramolecular OH repulsion by Mathew et al.

2.2.3 Gee FF (Revised)

The Gee FF¹⁰ was originally developed in 2004 using a proprietary closed-source software suite, which has led to some ambiguities in its implementation in other codes such as LAMMPS. Nonbonded interactions in the Gee FF are modeled using the Lennard-Jones form

$$U_{\text{NB}}^{\text{Gee}}(r) = \sum_{\text{pairs}} 4\epsilon_{\alpha\beta} \left[\left(\frac{\sigma_{\alpha\beta}}{r} \right)^{12} - \left(\frac{\sigma_{\alpha\beta}}{r} \right)^6 \right] + \frac{q_{\alpha}q_{\beta}}{4\pi\epsilon_0 r}, \quad (4)$$

where α and β again denote specific atom types on the well-depth ($\epsilon_{\alpha\beta}$) and zero crossing-point ($\sigma_{\alpha\beta}$) of the potential. Both $\epsilon_{\alpha\beta}$ and $\sigma_{\alpha\beta}$ were determined for heteroatom pairs using geometric means as mixing rules. It should be noted that the Bedrov FF and the Gee FF use different partial atomic charges. The Gee FF adopted generic DRIEDING FF parameters⁶⁹ for all harmonic bond and angle potentials along with a subset of the dihedral potentials. Quantum chemistry calculations⁷⁰ at the MP2/6-311G** level were used to parameterize the C-C-N-O and C-C-N-H dihedrals that account for rotations of the nitro and amine groups.

Perhaps the greatest ambiguity in the implementation of the Gee FF concerns its choice for intramolecular pairwise exclusions. The original report specifies that all 1-2 and 1-3 pairs were excluded and that “all intramolecular N-C · · · H-N (sic) nonbonded interactions were also excluded.” In private correspondence with the lead author of that study, we obtained an example LAMMPS input deck in which these exclusions were implemented through the definition of fictitious zero-strength bonds between O and H atoms on adjacent nitro and amine groups. These fictitious bonds were only defined between O and H atoms that lie adjacent to each other in the crystal phase and were thus not invariant to rotations of the

nitro/amine groups. In our revised version of the Gee FF, we define the same intramolecular OH repulsive term between all distinct O-H pairs as is used for the Bedrov FF. It should be noted that this choice, combined with the default treatment in LAMMPS to use the *complete* list of topological bonds for defining a set of 1-2 and 1-3 exclusions, effectively leads to the exclusion of most intramolecular nonbonded interactions involving the N, O, and H atoms within/between all the nitro and amine groups. Included intramolecular nonbonded interactions are tabulated in the Supporting Information.

As a final note, our LAMMPS implementation of the Revised Gee FF involves redundant definitions for the C-C-N-O and C-C-N-H dihedrals, thus enabling rotational invariance of the nitro and amino group torsions. That is, for every nitro/amine torsion, there are four distinct topological dihedrals defined in the FF. To reconcile this redundancy with the quantum-chemistry predicted energy barriers for rotations of those groups, we scaled the dihedral force constants by a factor of 0.25 relative to Gee et al. report.

2.2.4 CLM FF

The first primary aim of this work is to parameterize a nonreactive FF for TATB that corrects inaccuracies in the high-pressure equation of state as predicted by the Bedrov FF. In two concurrent reports from 2022 (Refs. 14 and 15), it was found that the isothermal pressure-volume (PV) response of TATB crystal at room temperature was too compliant above ≈ 10 GPa compared to recent experiments by Plisson et al.¹⁶ In our efforts to arrive at a new TATB FF, we implemented and tested the Gee FF and found that it was too stiff at high pressure (see Sec. 3.2.1). This fact, together with inaccuracies in the Gee FF predictions for the vibrational density of states (see Sec. 3.1.1), prompted us to try merging the Bedrov FF with our revised version of the Gee FF. As will be shown at length below, this merger successfully improves many of the inaccuracies in the predicted TATB equation of state. We denote this new merged FF as the CEA-LLNL-Missouri FF (or CLM FF).

The CLM FF merges the covalent terms from the Bedrov FF with the nonbonded inter-

Table 1: CLM FF Parameters.

Nonbonded	Type	q (e)	ϵ (kcal·mol ⁻¹)	σ (Å)
	C(NO ₂)	0.2535	0.01	3.83086
	C(NH ₂)	-0.2175	0.01	3.83086
	N(O ₂)	0.6900	0.01	3.83086
	N(H ₂)	-0.7320	0.01	3.83086
	O	-0.4300	0.60	2.67270
	H	0.4330	0.20	1.51453
Bonds	Type	k_{bnd} (kcal·mol ⁻¹ ·Å ⁻²)	r_0 (Å)	
	C-C	500	1.440	
	C-N(O ₂)	300	1.427	
	C-N(H ₂)	672	1.322	
	N-O	878	1.230	
	N-H	850	1.010	
Angles	Type	k_{ang} (kcal·mol ⁻¹ ·rad ⁻²)	θ_0 (deg.)	
	C-C(NH ₂)-C	64	118.4	
	C-C(NO ₂)-C	64	121.6	
	C-C-N(H ₂)	60	121.7	
	C-C-N(O ₂)	60	119.2	
	C-N-O	140	116.8	
	C-N-H	64	112.0	
	O-N-O	95	117.3	
	H-N-H	64	119.0	
Dihedrals	Type	k_{dih} (kcal·mol ⁻¹)		
	C-C-C-C	5.35		
	C-C-C-N	20.0		
	N-C-C-N	20.0		
	C-C-N-O	1.60		
	C-C-N-H	8.88		
Improper	Type	k_{imp} (kcal·mol ⁻¹)		
	C-C-C-N*	36.5		
	O-N-O-C*	89.3		
	H-N-H-C*	2.10		

actions from the Revised Gee FF. Specifically, we took all covalent bond, angle, dihedral, and improper terms from the Bedrov FF. The respective functional forms for these potentials are

$$U_{\text{bnd}}(r) = \frac{1}{2}k_{\text{bnd}}(r - r_0)^2, \quad (5)$$

$$U_{\text{ang}}(\theta) = \frac{1}{2}k_{\text{ang}}(\theta - \theta_0)^2, \quad (6)$$

$$U_{\text{dih}}(\phi) = \frac{1}{2}k_{\text{dih}}[1 - \cos(2\phi)], \quad (7)$$

$$U_{\text{imp}} = \frac{1}{2}k_{\text{imp}}\phi^2. \quad (8)$$

All repulsion-dispersion terms and the Coulombic partial charges were taken from the Revised Gee FF, which has the potential form given in Equation 4. The CLM FF also adopts the intramolecular OH repulsion term discussed above (Equation 2), along with its implications for nonbonded pairwise exclusions. Parameters for the CLM FF are collected in Table 1.

2.3 Reactive Force Fields

The second primary aim of this work is to provide a comprehensive validation test of widely used FFs for TATB. Two reactive FFs based on the ReaxFF energy function find frequent application to TATB.⁷¹⁻⁷⁷ These two parameterizations are ReaxFF-LG¹² and ReaxFF-2018,¹³ both of which have been specifically developed for modeling high explosives, although not necessarily TATB. It should be noted that both ReaxFF versions include corrections for London dispersion, which leads to improved density predictions relative to the earlier versions of ReaxFF on which these two variants are based.

Simulations with the above ReaxFF variants were performed using the “reax/c” module in the 29Sep2021 version of LAMMPS. Partial charges were determined at each timestep using the QEq charge equilibration scheme⁷⁸ with an accuracy tolerance of 10^{-6} . All choices for thermostats, barostats, and other property-specific calculation methods were the same as for our nonreactive FF MD simulations. We note that the computational cost of ReaxFF

does not scale linearly with the particle count and is substantially more computationally expensive than our nonreactive FF calculations. Thus, in some instances we integrated shorter trajectories with ReaxFF compared to those obtained with the nonreactive FFs. We also note that geometry optimizations were generally more difficult to converge with ReaxFF, and in particular with ReaxFF-LG, compared to the nonreactive FFs. Several instances where we were unable to successfully optimize structures with ReaxFF are noted in the Results and Discussion.

3 Results and Discussion

3.1 Molecular Properties

3.1.1 Vibrational Density of States

Accuracy of the FF descriptions of the intramolecular potential energy surface was assessed through a comparison of the molecular vibrational density of states (VDOS), which is constrained by experiments for TATB. The VDOS provides a sensitive measure of the fundamental vibrational frequencies of the molecule (i.e., peak positions), which directly tests the accuracy of a FF's description of the curvature of the $3N$ -dimensional potential energy surface near the ground state. The associated vibrational lifetimes (i.e., peak widths) that arise from anharmonic mode couplings are also measured by the VDOS, but these correspond to the result in the classical limit due to the use of classical equations of motion. Hence, in what follows we focus primarily on the peak positions.

Figure 2 shows the predicted isothermal VDOS of isolated TATB molecules at 300 K in comparison to three different experiments. The FF VDOS predictions were obtained from the last 50 ps of a 100 ps long NVT trajectory performed for a single molecule in a large cubic cell of side length 30 Å. Configuration snapshots were sampled every 0.5 fs and were post-processed using the TRAVIS code⁷⁹ to obtain the mass-weighted VDOS. It should be

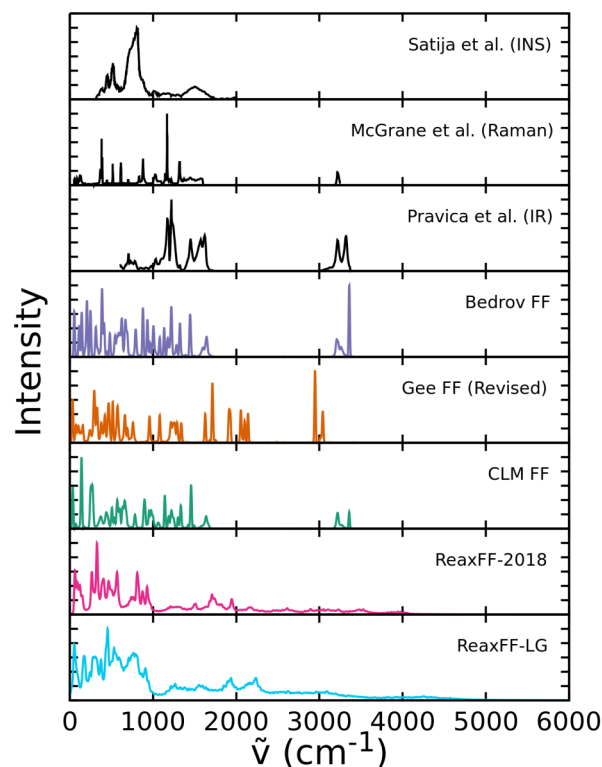


Figure 2: Comparison of FF predictions for the vibrational density of states of an isolated TATB molecule at 300 K to the TATB crystal vibrational spectra determined experimentally at room temperature and pressure by Satija et al.,³² McGrane et al.,³⁴ and Pravica et al.³⁵

noted that this yields the complete VDOS, irrespective of any selection rules or scattering cross-sections. The three experiments all correspond to TATB crystal at room temperature and atmospheric pressure and include the inelastic neutron scattering (INS) measurements of Satija et al.,³² the Raman measurements of McGrane et al.,³⁴ and the infrared (IR) measurements of Pravica et al.³⁵ Of the three, only INS measures the VDOS peak positions absent any selection rules, but intensities are weighted towards modes involving hydrogen and those experiments did not probe the high-frequency regime above $\approx 2000 \text{ cm}^{-1}$. Hence, the Raman and IR measurements are the only ones that capture the peaks above 3000 cm^{-1} that are associated with the amine N-H stretching motions.

Focusing first on the nonreactive FFs, it can be clearly seen that the Bedrov FF does an excellent job of capturing the mid- and high-frequency peak positions above $\approx 1400 \text{ cm}^{-1}$ for which it was trained.⁵² This includes the splitting of the three symmetric and three

antisymmetric N-H peaks respectively at $\approx 3200\text{ cm}^{-1}$ and $\approx 3300\text{ cm}^{-1}$. Intramolecular vibrational accuracy is also largely inherited by the CLM FF, which takes its covalent FF parameters from the Bedrov FF. One can also clearly see the negative consequences of the Revised Gee FF's adoption of generic DRIEDING FF covalent potentials. The Revised Gee FF exhibits a number of peaks between 1600 and 3200 cm^{-1} where all of the experiments show zero signal.

While the Gee FF exhibits errors compared to experiments, these errors are generally modest compared to the qualitatively inaccurate VDOS predicted by both ReaxFF potentials. Both ReaxFF versions exhibit spectral intensity across a broad range of frequencies including in the region between 1600 and 3200 cm^{-1} . There is non-zero intensity at frequencies as high as $\approx 4000\text{ cm}^{-1}$ with ReaxFF-2018 and as high as $\approx 5000\text{ cm}^{-1}$ with ReaxFF-LG. Both spectra show a general lack of well-defined narrow peaks, which may indicate that the intramolecular vibrational coupling is exceptionally strong with both potentials. It is also worth noting that we were unable to perform a normal mode analysis with ReaxFF-LG (unlike for the other FFs) as we were unable to obtain an optimized TATB structure that was free of saddle points (i.e., negative eigenfrequencies).

It is difficult to anticipate all of the consequences of inaccuracies in the VDOS for predictions of other properties, but there are a few physical and chemical properties worth noting. First, nonreactive energy transfer processes are likely impacted. These include intramolecular vibrational relaxation that is important to the description of phonon up-pumping⁸⁰ and the thermal conductivity.⁸¹ Reactive processes are also sensitive to the VDOS. From the perspective of transition state theory, chemical kinetics will depend on the attempt frequency in the reactant state, which is directly related to the mode frequencies. It is also highly plausible that anharmonic features on the potential energy surface, which give rise to the peak widths, also affect the attempt frequency and the local topology of the surface near transition states. The importance of the above physics to describing TATB thermo-mechanical and chemical responses under extreme conditions provides strong motivation for

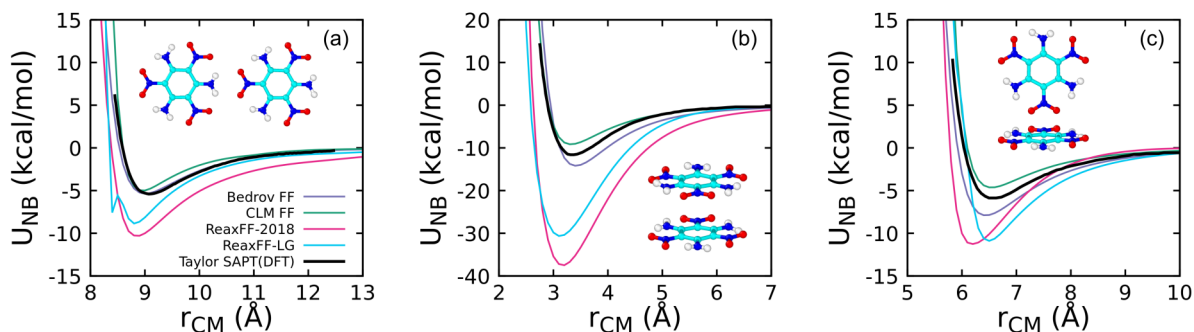


Figure 3: Rigid-body dimer energies obtained using the Bedrov FF, CLM FF, ReaxFF-2018, and ReaxFF-LG compared to the electronic structure predictions of Taylor.⁴⁰ Inset images in each panel show the selected dimer orientation and plot the total nonbonded interaction potential energy U_{NB} as a function of r_{CM} , the relative displacement between molecular centers of mass. Note that the CLM FF yields identical predictions to the Gee FF (Revised) as these two FFs have identical intermolecular terms.

explicitly training or validating future TATB FFs against the experimental VDOS.

3.1.2 Dimer Energies

Accuracy of the FF descriptions of the intermolecular potential energy surface was assessed through a comparison of dimer energies. Taylor showed⁴⁰ that a rigid-molecule TATB FF trained exclusively to high-level symmetry-adapted perturbation theory (SAPT) DFT calculations of dimer energy landscapes could accurately reproduce experimental measurements of TATB crystal structure, thermal expansion, sublimation enthalpy (i.e., crystal binding energy), and bulk modulus. This indicates that tests of the dimer energy landscape provide a good proxy for obtaining accurate properties of the crystal.

We extracted a subset of Taylor's data for comparison and performed analogous rigid-body calculations using the FF models, which are shown in Figure 3. Because of the rigid-body approximation, these calculations effectively isolate U_{NB} from the total potential. It should be noted that the Revised Gee FF and CLM FF yield identical results, so only curves for the CLM FF are shown. Taylor made the choice to use TATB molecular geometries as determined by Cady and Larson¹ for TATB crystal, which exhibit subtle breaking of D_{3h} symmetry. We attempted to match this choice and the specific dimer orientations as closely

as possible and therefore only show three such dimer “scans” that can be unambiguously reproduced.

The dimer scan in panel (a) tests the energy landscape for interactions within the TATB crystal layers. Thus, one might anticipate that the features of the energy surface for this orientation will have a strong bearing on the accuracy of the a and b lattice lengths and intralayer spacing. It is perhaps surprising that the Bedrov FF reproduces the DFT results almost exactly, including the location of the potential energy minimum and the curvature along the entire surface. The CLM FF also performs well, although the minimum is at slightly smaller separation distance and the repulsive wall is somewhat stiffer. Both ReaxFF models predict substantially deeper minima, indicating that those models are overbound within the crystal layers by roughly a factor of two. It is also worth noting that ReaxFF-LG exhibits a discontinuity on this surface, which may be related to our difficulties in obtaining optimized geometries with that model.

In contrast, the dimer scan in panel (b) provides a good test for TATB binding along the layer stacking direction. Here, the Bedrov and CLM FF yield similar results to DFT, with the former being slightly overbound and the latter being slightly underbound. While both ReaxFF surfaces are smooth, they are substantially overbound in this direction by roughly a factor of three to four. The locations of the minima for the ReaxFF surfaces are also at shorter separation distance than DFT. Thus, one might expect that both ReaxFF models will predict crystal layer separation distances, $d_{(002)}$, that are smaller than experiment.

The last dimer scan in panel (c) does not correspond to a geometry found in TATB crystal, but may be encountered in disordered states such as the liquid or shear bands. Again, the Bedrov and CLM FFs yield similar results to DFT, but the agreement is decidedly worse than was seen for the scans in (a) and (b). Both ReaxFF models also overpredict the well depths by a larger margin than the nonreactive FFs. The separation distance at the potential minimum is in decent agreement with DFT for the CLM FF and ReaxFF-LG.

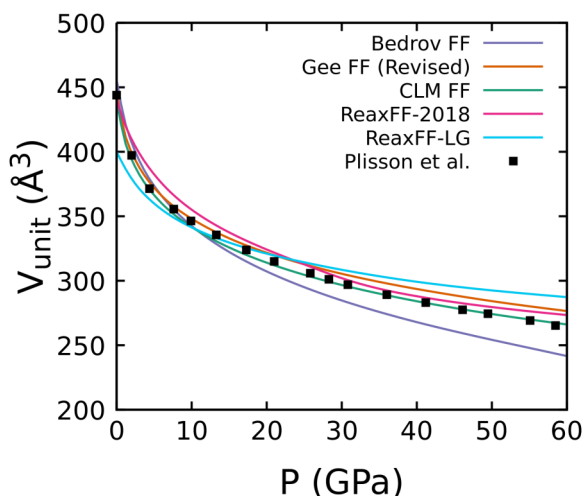


Figure 4: Predicted pressure-volume response of the triclinic $P\bar{1}$ TATB unit cell at 300 K compared to the diamond anvil cell experiments of Plisson et al.¹⁶

3.2 Equation of State of the Triclinic Phase

3.2.1 Isothermal Response at Room Temperature

Inaccuracies in the room-temperature isothermal pressure-volume (PV) response predicted by the Bedrov FF first identified in Refs. 14 and 15 were the initial motivation for our efforts to obtain a better TATB FF. The Bedrov FF was validated against the highest-pressure data available at the time, namely the 2008 diamond anvil cell experiments of Stevens et al.¹⁷ that went to 13 GPa. In 2017, Plisson et al.¹⁶ determined the room-temperature TATB PV response up to 66 GPa from an indexing of X-ray diffraction data to the triclinic $P\bar{1}$ space group. Subsequent single-crystal diffraction experiments performed in 2019 showed that TATB can undergo a subtle phase transition to a monoclinic $I2/a$ space group at ≈ 4 GPa.³¹ While there is some conjecture that the $I2/a$ phase exhibits a somewhat stiffer compression response, indexing the diffraction data to the $P\bar{1}$ space group yields similar PV responses between the two forms.⁸² Thus, we take the data of Plisson et al. as a benchmark for comparison of the FF predictions for the PV response and lattice parameters of the triclinic $P\bar{1}$ phase.

We predicted the PV response of triclinic TATB crystal at 300 K up to 60 GPa using

NVT and *NPT* simulations and an $8\times 8\times 12$ crystal supercell. These simulations started from the 30 GPa crystal structure of Plisson et al. and were split into three stages that were designed to suppress layer sliding defects that can arise at low pressure⁵³ due to the low stacking fault energies for basal glide.^{44,45} (See the Section 1 of the Supporting Information for additional discussion.) First, the crystal was thermalized at 300 K for 20 ps using *NVT* dynamics. Second, the crystal was taken to a specified pressure state using *NPT* dynamics over 100 ps through a linear pressure ramp. Third and finally, the crystal was held under *NPT* conditions at the target pressure for 400 ps and the equilibrium lattice parameters were obtained as a time average over the last 200 ps. As a final verification, short 100 ps *NVT* simulations were performed with new crystal supercells constructed using the *NPT*-average lattice parameters to check that the resulting stresses were hydrostatic at the specified pressure. It should be noted that the ReaxFF simulations were shortened by a factor of ten at each stage (except the initial *NVT* thermalization) due to their computational cost, and that the corresponding lattice parameters thus obtained should be viewed as only quasi-steady equilibrium values. Predictions for the *PV* response at 300 K are compared to the experiments of Plisson et al. in Figure 4 and the corresponding lattice parameters at 0, 30, and 60 GPa are given in Table 2.

Focusing first on the *PV* response, one can clearly see that the Bedrov FF is too compliant at high pressure, underpredicting the unit cell volume V_{unit} by 9% at 60 GPa. This contrasts with the excess stiffness in the Revised Gee FF. While ReaxFF-2018 exhibits some error at pressures below 20 GPa, it captures the response at higher pressures better than any FF besides the new CLM FF. ReaxFF-LG exhibits a distinctly different trend than the experiments, yielding a substantially smaller V_{unit} than experiment at 0 GPa and the largest V_{unit} among the FF models at 60 GPa. This indicates that ReaxFF-LG does not accurately capture TATB's pressure-dependent bulk modulus. Perhaps serendipitously, the CLM-FF, which is an ad hoc merger of the Bedrov FF and Revised Gee FF, yields excellent agreement with Plisson et al. across the entire pressure range.

Table 2: Lattice parameters of the $P\bar{1}$ phase of TATB determined at room temperature and selected pressures.

Source	a (Å)	b (Å)	c (Å)	α (deg.)	β (deg.)	γ (deg.)	V_{unit} (Å ³)	$d_{(002)}$ (Å)
0 GPa								
Plisson et al. ¹⁶	9.040	9.030	6.810	108.5	91.7	120.0	443.8	3.143
Cady and Larson ¹	9.010 (-0.3) ^a	9.028 (0.0)	6.812 (0.0)	108.6 (0.1)	91.8 (0.1)	120.0 (0.0)	442.5 (-0.3)	3.140 (-0.1)
Kolb and Rizzo ¹⁸	9.017 (-0.3)	9.047 (0.2)	6.815 (0.1)	108.6 (0.1)	91.9 (0.2)	120.0 (0.0)	442.9 (-0.2)	3.139 (-0.1)
Sun et al. ¹⁹	9.016 (-0.3)	9.033 (0.0)	6.827 (0.2)	108.7 (0.2)	91.8 (0.1)	120.0 (0.0)	443.7 (0.0)	3.145 (0.1)
Bedrov FF	9.015 (-0.3)	9.070 (0.4)	7.072 (3.8)	114.1 (5.2)	80.8 (-11.9)	120.1 (0.1)	455.7 (2.7)	3.222 (2.5)
Gee FF (Revised)	8.940 (-1.1)	8.979 (-0.6)	7.073 (3.9)	113.2 (4.3)	85.7 (-6.5)	120.1 (0.1)	446.3 (0.6)	3.212 (2.2)
CLM FF	8.900 (-1.5)	8.937 (-1.0)	6.947 (2.0)	111.3 (2.6)	86.7 (-5.4)	120.0 (0.0)	440.4 (-0.8)	3.197 (1.7)
ReaxFF-2018	9.225 (2.1)	9.221 (2.1)	6.581 (-3.4)	111.1 (2.4)	90.1 (-1.7)	120.0 (0.0)	440.8 (-0.7)	2.991 (-4.8)
ReaxFF-LG	8.926 (-1.3)	8.926 (-1.2)	7.223 (6.1)	105.8 (-2.5)	108.7 (18.5)	120.1 (0.1)	400.0 (-9.9)	2.903 (-7.6)
30 GPa								
Plisson et al. ¹⁶	8.520	8.400	5.422	113.7	90.4	119.9	297.0	2.396
Bedrov FF	8.068 (-5.3)	8.134 (-3.2)	5.620 (3.6)	110.8 (-2.5)	94.3 (4.4)	119.7 (-0.2)	284.7 (-4.1)	2.497 (4.2)
Gee FF (Revised)	8.446 (-0.9)	8.463 (0.7)	5.574 (2.8)	113.7 (0.0)	90.3 (-0.1)	119.9 (0.0)	305.4 (2.8)	2.465 (2.9)
CLM FF	8.280 (-2.8)	8.300 (-1.2)	5.580 (2.9)	112.7 (-0.9)	90.7 (0.4)	119.8 (-0.1)	296.7 (-0.1)	2.488 (3.9)
ReaxFF-2018	8.672 (1.8)	8.693 (3.5)	5.291 (-2.4)	113.2 (-0.5)	92.4 (2.2)	120.3 (0.3)	302.0 (1.7)	2.319 (-3.2)
ReaxFF-LG	8.615 (1.1)	8.666 (3.2)	5.541 (2.2)	116.0 (2.1)	90.5 (0.1)	119.8 (-0.1)	308.5 (3.9)	2.381 (-0.6)
60 GPa								
Plisson et al. ¹⁶	8.240	8.170	5.130	114.2	89.8	119.6	265.3	2.265
Bedrov FF	7.503 (-8.9)	7.606 (-6.9)	5.368 (4.6)	107.9 (-5.5)	97.8 (8.9)	118.4 (-1.0)	241.6 (-8.9)	2.405 (6.2)
Gee FF (Revised)	8.241 (0.0)	8.241 (0.9)	5.319 (3.7)	113.6 (-0.5)	90.5 (0.8)	120.0 (0.3)	276.5 (4.2)	2.351 (3.8)
CLM FF	8.026 (-2.6)	8.032 (-1.7)	5.338 (4.0)	112.6 (-1.4)	90.9 (1.2)	119.9 (0.2)	266.1 (0.3)	2.379 (5.1)
ReaxFF-2018	8.555 (3.8)	8.560 (4.8)	5.004 (-2.5)	114.2 (0.0)	92.8 (3.3)	120.2 (0.5)	273.4 (3.0)	2.161 (-4.6)
ReaxFF-LG	8.477 (2.9)	8.559 (4.8)	5.418 (5.6)	118.1 (3.4)	89.7 (-0.1)	119.8 (0.1)	287.3 (8.3)	2.281 (0.7)

^aRelative percent error measured with respect to Plisson et al.

More detailed inspections of the 0 GPa lattice parameters in Table 2 reveals a number of trends. First, it should be noted that the data of Plisson et al. agree to within 0.3% when compared against the older determinations by Cady and Larson¹ from 1965, by Kolb and Rizzo¹⁸ from 1979, and by Sun et al.¹⁹ from 2010. The lattice parameters from the Revised Gee FF and the CLM FF are also quite similar to each other, which indicates that modifications to the intramolecular potential terms only serve as a minor perturbation. It is also clear that the three nonreactive FFs all yield reasonable intralayer and interlayer spacings relative to experiment. (Note that while a and b are good measures of intralayer spacings, $d_{(002)}$ is a clearer metric for interlayer spacing as lattice parameters c , α , and β are convolved with each other and with shifts of the layers in the directions lateral to the layer normal.) In contrast, while both ReaxFF models predict reasonable intralayer spacings (a and b), the interlayer spacing is much smaller. This is likely related to features of the dimer energy scan seen in Figure 3(b). All FFs yield a $V_{\text{unit}}(0 \text{ GPa})$ that is within 3% of experiment except for ReaxFF-LG, which deviates by 10%.

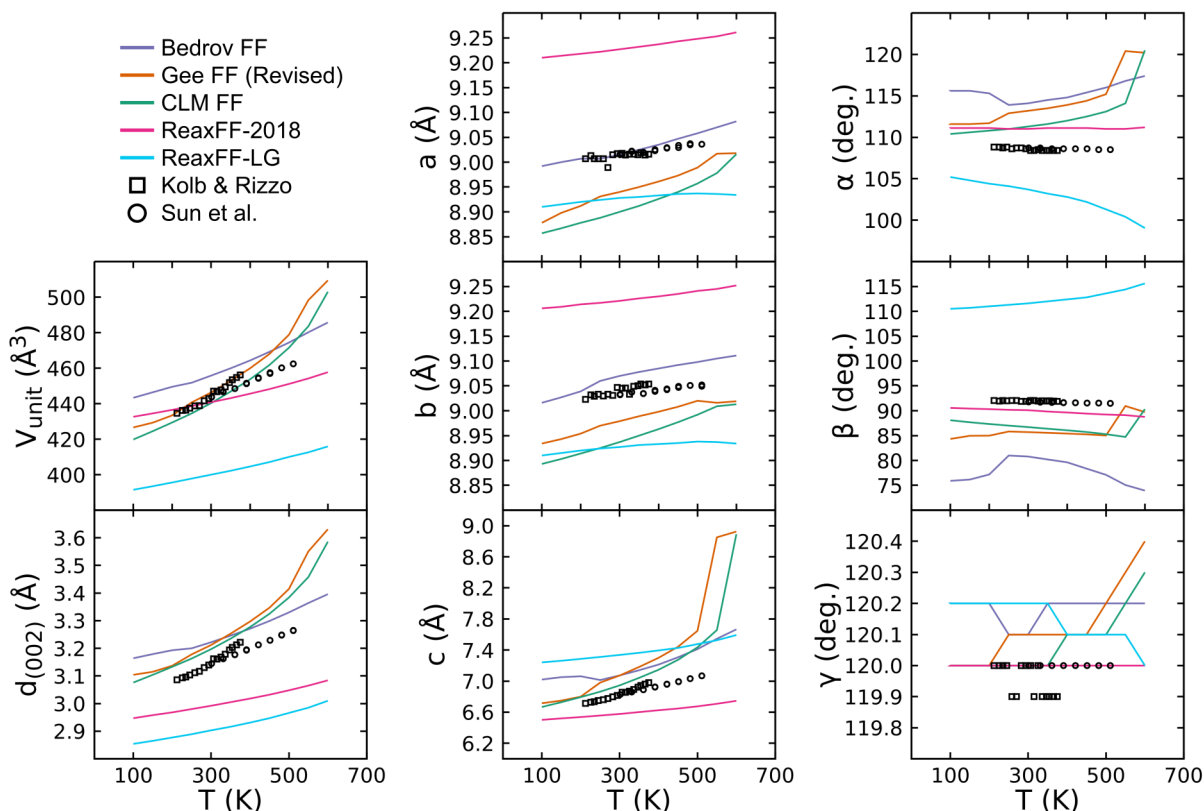


Figure 5: Predicted temperature dependence of the $P\bar{1}$ TATB lattice parameters at atmospheric pressure compared to the experiments of Kolb and Rizzo¹⁸ and Sun et al.¹⁹

The lattice parameters at higher pressures reveal a number of additional features not immediately discernible in Figure 4. For instance, while ReaxFF-2018 does a good job capturing the PV response, the values for a , b , and $d_{(002)}$ reveal that the agreement at high pressure is largely due to a cancellation of errors between intralayer and interlayer spacings. A similar, but more modest cancellation of errors is also apparent with the CLM FF. At the same time, the overcompliance of the Bedrov FF largely stems from it being too compressible along a and b . It is also not surprising based on the PV curves that errors in the lattice parameters predicted by ReaxFF-LG are generally larger than with the other FF models.

3.2.2 Isobaric Response at Atmospheric Pressure

Anisotropic thermal expansion of TATB crystal at atmospheric pressure is a well-documented^{18,19} and has been invoked to explain composite-scale phenomena such as ratchet growth in which thermal cycling leads to the formation of additional porosity in TATB-based HE formulations.⁸³ Linear thermal expansion coefficients for the c lattice parameter are measured to be between 17-30 times larger than for the a and b lattice parameters.^{18,19} At the same time, the underlying lattice parameter data used to compute thermal expansion coefficients serves as a useful benchmark for testing a basic anharmonic material property with these FFs.

We obtained the 0 GPa lattice parameters using the FFs for temperatures $T \in [100 \text{ K}, 600 \text{ K}]$ in 50 K increments following the same protocol as above for the isothermal PV response, with the only exception being the substitution of a linear temperature ramp rather than a pressure ramp. The resulting temperature-dependent lattice parameters are plotted in Figure 5 in comparison to the experiments of Kolb and Rizzo¹⁸ and Sun et al.¹⁹ It is apparent from the plots that none of the FFs simultaneously capture all of the experimental data across all of the lattice parameters.

Focusing on the volume, both the Revised Gee FF and the CLM FF capture experiments with quantitative accuracy, although the associated slope (and therefore thermal expansion coefficient) most closely aligns with the experiments of Kolb and Rizzo. The Bedrov FF overpredicts the volume, but exhibits a slope that is close to the data of Sun et al. ReaxFF-2018 also predicts the volume with good quantitative accuracy. In contrast, while ReaxFF-LG predicts a reasonable temperature functional dependence, the absolute values are substantially lower than either experiment across the entire temperature range.

Inspection of the intralayer and interlayer spacings given by a , b , and $d_{(002)}$ reveal that the nonreactive FFs are generally more accurate than either of the ReaxFF models. In particular, the Bedrov FF most accurately captures the intralayer spacing (a and b) and exhibits similar accuracy for the $d_{(002)}$ interlayer spacing as the Revised Gee FF and the CLM FF. Both ReaxFF models underpredict $d_{(002)}$, but show opposing trends for a and

b, with ReaxFF-2018 predicting larger interlayer spacing than experiment and ReaxFF-LG predicting smaller values.

Lattice parameters *c*, α , and β exhibit a number of unusual features. For instance, the CLM-FF exhibits an abrupt change in these parameters above 500 K. Inspection of the trajectory configurations (not shown) reveals that the crystal undergoes some sort of structural solid-solid transition in this range. While the lattice parameters have not been conclusively determined in experiments at these high temperatures, this response is qualitatively consistent with experimental measurements of second harmonic generation, which have been posited to be induced by some sort of pre-reactive structural transition.^{29,84–86} Non-monotonic responses are seen below 300 K with the Bedrov FF. While ReaxFF-2018 is the most accurate for all three lattice angles (α , β , and γ), such agreement is arguably less important for accurately modeling TATB EOS than are the parameters associated with lattice spacings. All FFs predict that the intralayer packing is essentially hexagonal (i.e., $\gamma \rightarrow 120^\circ$), consistent with experiments.

3.3 Transformations to Other Phases

3.3.1 Solid-Gas

TATB exhibits particularly low volatility, even at high temperatures of 400-450 K, with typical vapor pressures on the order of $1\text{-}100 \times 10^{-7}$ torr ($\approx 1\text{-}100 \times 10^{-10}$ atm).²⁶ Despite this, the single peer-reviewed experimental determination of the sublimation enthalpy ΔH_{sub} for TATB by Rosen and Dickinson²⁶ provides a useful benchmark for the crystal binding energy, which can be readily computed from MD simulations. We determined ΔH_{sub} as

$$\Delta H_{\text{sub}} = \langle E_{\text{gas}} \rangle_{NVT} - \langle E_{\text{crystal}} \rangle_{NVT} + RT, \quad (9)$$

where E_{gas} and E_{crystal} are respectively the total energies (per molecule) of an isolated TATB molecule and TATB crystal, $\langle f \rangle_{NVT}$ denotes a (time) average of property *f* in the canonical

Table 3: TATB crystal sublimation enthalpy.

Source	ΔH_{sub} (kcal·mol ⁻¹)
Rosen and Dickinson ²⁶	40.2
Garza ²⁷	43.1 (7.2) ^a
Bedrov FF	40.4 (0.5)
Gee FF (Revised)	35.1 (-12.7)
CLM FF	34.2 (-14.8)
ReaxFF-2018	60.5 (50.4)
ReaxFF-LG	69.9 (73.8)

^aRelative percent error measured with respect to Rosen and Dickinson.

(*NVT*) ensemble, and R is the ideal gas constant. The average energies were both obtained through *NVT* MD simulations 300 K, with the crystal energy deriving from an $8 \times 8 \times 12$ supercell in a hydrostatic state at 1 atm. The resulting ΔH_{sub} values are collected in Table 3. We also include for completeness the experimental result by Garza from a non-peer-reviewed 1979 LLNL technical report.²⁷

The Bedrov FF accurately reproduces the experimental result, essentially by design, as its repulsion and dispersion interaction potentials were empirically adjusted to reproduce this result.¹¹ Both the Revised Gee FF and the CLM FF modestly underpredict ΔH_{sub} by a factor of no more than 15%. In contrast, both ReaxFF models predict much larger values for ΔH_{sub} than experiment, and thus yield much more tightly bound crystals. The large ΔH_{sub} obtained with ReaxFF are qualitatively consistent with the large negative dimer interaction energies evidenced by the well depths in Figure 3.

It should be noted that the original ReaxFF-LG paper¹² reported $\Delta H_{\text{sub}} = 37.72$ kcal·mol⁻¹, which is roughly a factor of two smaller than our result ($69.9/2 = 34.95$). While we cannot explain this discrepancy, many details in the earlier study are unclear. In particular, cell angles were not reported for TATB and the *PV* response was obtained from short 10 ps *NVT* simulations (not *NPT* simulations). One conjecture is that the rough factor of two difference may arise from both a bookkeeping error (the TATB unit cell contains two molecules) and a non-hydrostatic stress state in the crystal.

Table 4: TATB crystal melting point at atmospheric pressure.

Source	T_m (K)
Bowlan et al. ²⁹	694
Stolovy et al. ²⁸	721 (3.9) ^a
Bedrov FF	830 (19.6)
Gee FF (Revised)	595 (-14.3)
CLM FF	585 (-15.7)

^aRelative percent error measured with respect to Bowlan et al.

3.3.2 Solid-Liquid

TATB does not have a chemically stable liquid phase, but several estimates of its melting point at atmospheric pressure are available in the literature. One of these is an older 1983 report by Stolovey et al.,²⁸ who determined a melting point of $T_m = 721$ K from a plateau in a temperature time history for a pressed-powder sample subjected to a fast (≈ 1 s) duration electron beam pulse. Very recently in 2022, Bowlan et al.²⁹ obtained an estimated melting temperature of $T_m = 694$ K. Their approach used time-resolved X-ray diffraction to quantify a kinetics model for loss of crystalline order due to chemical reactions, that when coupled with a thermodynamic model for melt acceleration kinetics yields the melting point as an asymptote.

We obtained corresponding estimates of T_m at atmospheric pressure for the three non-reactive FFs using the phase-coexistence approach. These simulations followed the same general simulation protocol as was applied to obtain the pressure-dependent melting curves for TATB,⁵¹ HMX,⁸⁷ and RDX.⁸⁸ Our simulations considered melting from the (100) crystal face and used a simulation cell that initially contained a $50 \times 5 \times 5$ crystal supercell (2500 molecules) in contact with a liquid region with 2500 molecules. A series of 10 ns long *NPT* trajectories were integrated at different temperatures to bracket the apparent T_m to within a 5 K increment. Upper bounds on the melting point were obtained by identifying the minimum temperature for which one or more crystal layers at the solid-liquid interface (out of the $50/2 = 25$ periodically distinct layers) lost rotational and translational order as identi-

fied by manual inspection of the trajectories. This yields a *kinetically effective* T_m . Tow et al.⁸⁹ showed for the explosive HMX that predictions for T_m based on phase coexistence,⁸⁷ which by design capture slowing of the kinetics as the melting point is approached from above, yield a modest and systematic offset of ≈ 50 K from the “true” thermodynamic melting point obtained from free energy based approaches. Resulting melting points are collected in Table 4.

In the case of the Bedrov FF, our simulations revealed partial melting of the crystal region at 830 K and partial crystallization of the liquid at 825 K. In contrast, the Revised Gee FF predicts partial melting of the crystal at temperatures as low as 595 K, but none of our simulations resulted in any crystallization of the liquid region. The CLM FF predicted melting at a somewhat lower temperature (585 K) than the Revised Gee FF, but we did identify partial crystallization of the liquid with the CLM FF at 560 K. We note here that the melting behavior of TATB is sensitive to finite size effects, with smaller 1000-molecule supercells containing a $10 \times 5 \times 5$ crystal predicting spontaneous liquid *crystallization* at temperatures that were up to 80 K higher than the *melting points* obtained with the large cells. Closer inspection of this possible nanoconfinement effect and a more detailed assessment of the melting kinetics are the subject of ongoing work.

All three FFs predict melting points that are within 16% of the value obtained by Bowlan et al. through their extrapolation scheme. The Bedrov FF overestimates T_m whereas both the Revised Gee FF and CLM FF underestimate T_m . Relative ordering of T_m predicted by each FF directly tracks with the predicted sublimation enthalpies ΔH_{sub} in Table 3. This is perhaps not surprising, as the sublimation enthalpy is the sum of the melting and vaporization enthalpies ($\Delta H_{\text{sub}} = \Delta H_{\text{melt}} + \Delta H_{\text{vapor}}$). It is also worth noting that differences between the Gee and CLM FFs indicate that the intramolecular potential has some bearing on T_m . Comparisons of the *PV* responses and the *a* and *b* lattice parameters indicate that the TATB molecule is somewhat more mechanically compliant with the CLM FF compared to the Revised Gee FF. Thus, the small differences in T_m predicted by these two FFs may

indicate that molecular flexibility plays a role in determining the melting point.

Our determinations here using the Bedrov FF yield a somewhat smaller value than was previously obtained with this FF by Mathew et al.⁵⁰ (851 K). The simulations of Mathew et al. were substantially smaller, starting from a $10\times 5\times 5$ crystal, and their trajectories were shorter (5 ns). Because the phase coexistence approach tracks melting dynamics, which can become very slow near T_m , it is not unreasonable that our larger and longer simulations yielded a lower upper bound on the melting point.

3.3.3 Solid-Solid

The recent 2019 single-crystal diffraction study by Steele et al.³¹ has provided some of the most conclusive evidence to date that TATB crystal can undergo structural solid-solid transitions. In particular, those authors identified a new monoclinic phase in the $I2/a$ space group that was related to the established triclinic $P\bar{1}$ phase via net translations of the crystal layers. This transition is essentially isochoric and occurs at ≈ 4 GPa. DFT calculations performed at the PBE-D2 level in that study indicated that the monoclinic and triclinic phases are approximately isenthalpic, but the free energy landscape for the transition remains unquantified.

To assess whether the various FFs can accurately describe the monoclinic phase, we performed NPT simulations to determine the pressure-dependent lattice parameters at 300 K and (meta)stability of the $I2/a$ form following the same general procedure as in Sec. 3.2.1. Resulting lattice parameters and the corresponding $I2/a$ primitive unit cell are shown in Figure 6. All FFs predict that the monoclinic and triclinic phases have essentially the same PV response, with the per-molecule volumes at each pressure differing by no more than 2 \AA^3 . Each FF except for ReaxFF-LG also predicts that the monoclinic phase is at least meta-stable on a timescale of 10s to 100s of ps, as no structural transitions (involving layer sliding or otherwise) occurred during the NPT trajectories. Thus, we were able to determine the monoclinic phase lattice parameters below the experimental transition pressure.

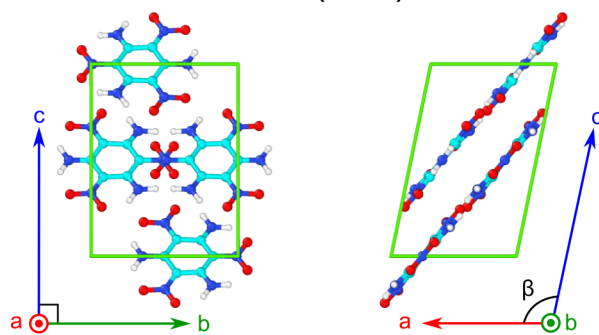
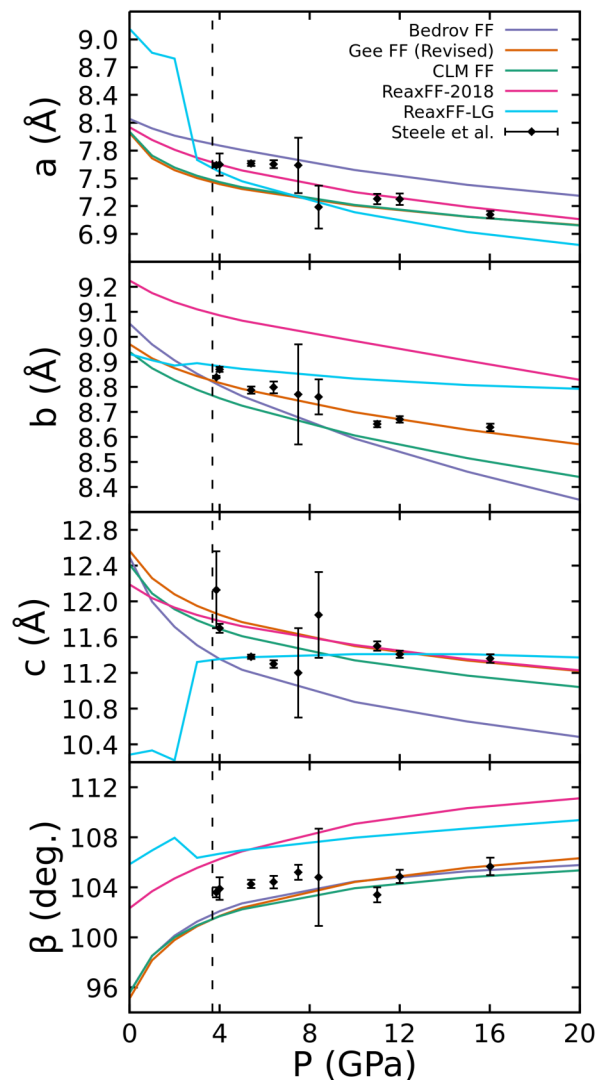


Figure 6: Predicted 300 K lattice parameters for the monoclinic $I2/a$ phase of TATB compared to the experiments of Steele et al.³¹ The phase transition pressure $P = 3.68$ GPa is denoted with a vertical dashed line. All FFs predict that the $I2/a$ phase is meta-stable below the experimental transition pressure. The $I2/a$ primitive unit cell contains four molecules and is shown at the bottom.

It is clear from the figure that each of the FFs is at least qualitatively consistent with experiment in describing the monoclinic phase above the experimental transition pressure. The CLM FF and Revised Gee FF are arguably the most accurate of the nonreactive FFs as the Bedrov FF consistently over- or underestimates each of the lattice parameters. ReaxFF-2018 does a good job capturing the pressure-dependent trend of lattice parameters a and c , but overestimates both b and β . ReaxFF-LG differs from all the other FFs in that it does not predict that the monoclinic form is metastable down to 0 GPa; it predicts a facile structural transition below 3 GPa, adopting triclinic lattice parameters (i.e., $\alpha \neq \gamma \neq 90^\circ$) and a packing structure (not shown) that is distinctly different from the the AB packing structure of the Cady and Larson $P\bar{1}$ form. While it is not clear from this data whether any of the FFs correctly *predicts* the triclinic \rightarrow monoclinic phase transition pressure, it nonetheless shows that these FFs can be reasonably applied to model the monoclinic phase at high pressure.

3.4 Elastic Mechanical Response

3.4.1 Benchmark Data and Calculation Details

The full second-order elastic tensor [C_{ij}] of TATB single crystal in the $P\bar{1}$ triclinic phase has previously been computed at 0 K within the quasi-harmonic approximation through planewave DFT calculations at the Perdew-Burke-Ernzerhof⁹⁰ (PBE) level by Rykounov³⁷ and Qin et al.³⁸ We note that Rykounov extensively tested the choice of dispersion correction, pseudopotentials, k -mesh density, and plane wave basis cutoff, and that they generally settled on more conservative choices for these parameters than did Qin et al. A subset of the C_{ij} were also computed by Valenzano et al.³⁶ using hybrid DFT and the quasi-harmonic approximation, but for a unit cell that was constrained to match the experimental volume at room temperature. Previous FF-based determinations of the full [C_{ij}] of the $P\bar{1}$ form have been computed using finite-temperature classical MD and hybrid MD-MC (Monte Carlo) techniques with variants of the Bedrov FF^{11,44,45} and the Gee FF.⁴³ As will be discussed extensively below, there is some disagreement within the literature data, even among the

Table 5: Elastic coefficients (in GPa) of the $P\bar{1}$ phase of TATB determined at 0 K and selected pressures.

Source	C_{11} (GPa)	C_{22} (GPa)	C_{33} (GPa)	C_{44} (GPa)	C_{55} (GPa)	C_{66} (GPa)	C_{12} (GPa)	C_{13} (GPa)	C_{23} (GPa)	K (GPa)	G (GPa)	E (GPa)	A_{univ} (Unitless)
0 GPa													
Rykounov (DFT)	83.20	78.30	18.90	1.70	1.50	30.00	21.90	-2.40	-0.30	18.79	10.48	26.52	20.14
Qin et al. (DFT)	82.04	79.75	19.43	19.91	14.64	34.18	11.05	5.17	11.87	21.59 (14.9) ^a	21.06 (100.9)	47.67 (79.8)	2.16 (-89.3)
This work (DFT)	79.59	78.49	19.02	2.36	2.66	34.24	19.16	-0.97	-0.18	18.58 (-1.2)	11.89 (13.5)	29.40 (10.9)	13.08 (-35.0)
Bedrov FF	62.13	60.82	21.55	1.58	0.34	22.41	20.09	3.15	5.33	18.75 (-0.2)	6.82 (-34.9)	18.26 (-31.2)	55.40 (175.2)
Gee FF (Revised)	109.23	100.72	20.50	2.26	2.46	36.15	29.92	4.03	4.51	25.31 (34.7)	12.93 (23.4)	33.15 (25.0)	17.53 (-13.0)
CLM FF	98.54	93.49	23.91	2.02	2.19	35.02	28.18	2.27	4.09	24.99 (33.0)	12.24 (16.8)	31.56 (19.0)	17.72 (-12.0)
Reaxff-2018	126.34	122.05	31.95	1.64	1.13	40.11	41.50	-0.23	0.32	31.27 (66.4)	13.71 (30.8)	35.89 (35.4)	37.63 (86.9)
Reaxff-LG	588.98	414.00	73.35	9.03	5.26	209.12	166.76	9.08	-8.53	68.57 (264.9)	47.33 (351.6)	115.43 (335.3)	-63.54 (-415.6)
10 GPa													
Rykounov (DFT)	257.00	249.50	130.50	15.20	13.30	90.00	77.60	26.60	29.30	93.57	42.68	111.14	5.35
Qin et al. (DFT)	-	-	-	-	-	-	-	-	-	92.60 (-1.0)	42.03 (-1.6)	129.98 (14.5)	-
Bedrov FF	147.70	141.83	101.96	5.48	3.01	39.71	66.03	27.77	31.51	68.92 (-26.3)	17.88 (-58.1)	49.38 (-55.6)	11.40 (113.0)
Gee FF (Revised)	271.60	260.57	119.18	9.85	8.01	80.68	106.99	31.73	32.95	99.16 (6.0)	35.09 (-17.8)	94.16 (-15.3)	9.24 (72.6)
CLM FF	220.86	218.58	121.12	9.31	7.30	69.51	83.20	30.27	31.70	88.52 (-5.4)	31.02 (-27.3)	83.33 (-25.0)	8.26 (54.4)
Reaxff-2018	203.22	401.93	105.75	0.80	9.27	152.28	88.08	-0.89	0.13	39.27 (-58.0)	36.42 (-14.7)	83.45 (-24.9)	-317.90 (-6041.7)
Reaxff-LG	919.56	570.87	193.75	4.99	23.39	183.00	513.89	122.03	144.30	263.35 (181.5)	108.11 (153.3)	285.28 (156.7)	0.68 (-87.3)
30 GPa													
Qin et al. (DFT)	-	-	-	-	-	-	-	-	-	188.55	77.59	232.02	-
Bedrov FF	214.16	222.76	237.15	9.43	4.61	47.84	126.90	80.60	78.46	138.08	25.60	72.32	9.78
Gee FF (Revised)	455.87	425.97	295.27	26.45	21.61	122.61	199.31	88.71	89.32	206.22	66.67	180.54	4.62
CLM FF	378.19	367.79	298.06	22.63	19.09	112.59	162.86	83.59	84.39	186.20	59.39	161.04	4.75

^aRelative percent error measured with respect to Rykounov.³⁷

different sets of the DFT-computed C_{ij} values.

In the present work, we computed the second-order elastic tensor at 0 K through DFT calculations using the same approach as in Ref. 16 as well as for each of the FFs. The DFT calculations were performed using the PBE functional⁹⁰ with Grimme D2 corrections⁹¹ and the projector augmented wave (PAW) formalism⁹² in the ABINIT code.⁹³ Additional DFT calculation details and the cell optimization process used to obtain FF predictions for the unit cell parameters at 0 K are described in Section 2 of the Supporting Information. Elastic coefficients were calculated at pressures of 0, 10 and 30 GPa with the FFs and at 0 GPa only with DFT. Our DFT calculations were performed to help determine which of the previous DFT-based reports to treat as a baseline for validating FF-based predictions. All comparisons are made in the standard rotational frame for the unit cell, for which lattice vector \mathbf{a} is aligned with x , lattice vector \mathbf{b} lies in the x - y plane, and lattice vector \mathbf{c} is oriented in the $+z$ half space.

Both the elastic coefficients computed in the present work and those from the literature for the 0 K state are reported in Table 5. Rykounov reported full C_{ij} data at both 0 and

10 GPa hydrostatic pressures whereas Qin et al. only provided values at ambient pressure. While tabulated C_{ij} at 10 GPa are missing from the Qin et al. study, those authors plotted the bulk (K), shear (G), and Young's (E) moduli up to 30 GPa computed with the Voigt-Reuss-Hill averaging scheme, which have been digitized and reported in Table 5. Finally, the universal anisotropy index⁹⁴ has been computed (when applicable) in order to compare the elastic anisotropy between the models, which is of crucial importance in the overall mechanical behavior of TATB single crystal as discussed in previous work.^{14,15,47}

3.4.2 Elasticity at 0 GPa

We first focus on the elastic coefficients at 0 GPa. One can immediately notice that there is modest spread in the C_{ij} among the FFs employed, with the exception of ReaxFF-LG, which is a clear outlier. As mentioned above, there is also considerable variation among the different DFT results.

Both Rykounov and Qin et al. predicted similar values for C_{11} , C_{22} , C_{33} and C_{66} while the latter obtained larger values for the out-of-plane shear elastic coefficients C_{44} and C_{55} that seem somewhat stiff considering TATB's loosely bound layered crystal structure. Rykounov obtained a C_{12} that was twice as large as Qin et al., while the former also predicted very small (and negative) values for C_{13} and C_{23} that are unlike the large positive values of the latter. While both studies obtained similar values for the bulk, shear, and Young's moduli, Rykounov's C_{ij} correspond to an elastic anisotropy that is ten times that of Qin et al. The comparatively small anisotropy index of Qin et al. is unusual considering the very anisotropic structure of TATB crystal.

Our DFT results are generally in better agreement with the data of Rykounov compared to Qin et al. Indeed, both our longitudinal and diagonal shear coefficients are very close to Rykounov, as well as C_{12} , which is related to the in-plane longitudinal stiffness coupling. Elastic coefficients C_{13} and C_{23} are somewhat dissimilar to Rykounov, but are still in much closer agreement than Qin et al. The fact that our DFT calculations more closely reproduce

the DFT results of Rykounov, together with the fact that Rykounov's study adopted more conservative DFT calculation parameters, indicates that that study may be the more reliable benchmark for comparison. To this end, all relative errors in Table 5 are computed with respect to Rykounov's results.

Compared to Rykounov's results, we find that the older FFs predict a number of major (and subtle) differences in the C_{ij} and derived moduli at 0 K and 0 GPa. As was discussed in previous studies,^{15,44,45} the Bedrov FF leads to generally smaller magnitude values compared to DFT, especially for in-plane longitudinal and shear coefficients that result in low shear and Young's moduli. Coefficients that are underpredicted by the Bedrov FF are generally overpredicted by the Revised Gee FF. Both of these nonreactive FFs yield errors in the moduli that do not exceed 35%. In contrast, both ReaxFF-2018 and ReaxFF-LG FFs predict that the crystal is very stiff, especially ReaxFF-LG for which both longitudinal and shear elastic coefficients look almost unrealistically large.

The CLM FF arguably provides the highest accuracy elastic coefficients at 0 K and 0 GPa among the various FFs. Elastic coefficients C_{11} , C_{22} , C_{12} , and C_{66} are lowered in comparison to the Gee FF values and increased in comparison to the Bedrov FF, which trends the results closer to (though still a bit higher than) the benchmark DFT data. In addition, the out-of-plane elasticity is reasonably reproduced and the homogenized elastic moduli are only slightly larger than the DFT results. Overall, the CLM FF predicts a more accurate elastic tensor than the other FFs with an elastic anisotropy index that is in good agreement with both the new DFT data and Rykounov's calculations.

In order to gain perspective on the directional elasticity of TATB single crystal, we used the full C_{ij} to compute 3D representations of the directional Young's ($E_{[hkl]}$) and shear ($G_{[hkl]}$) moduli, which are shown in Figure 7 for the CLM FF, our DFT calculations, and those by Rykounov. Such surfaces allow for direct insights into the elastic anisotropy of TATB single crystal. In the perfectly isotropic case, both Young's and shear moduli surfaces would be spheres, which is obviously not the case here. It is immediately clear that both

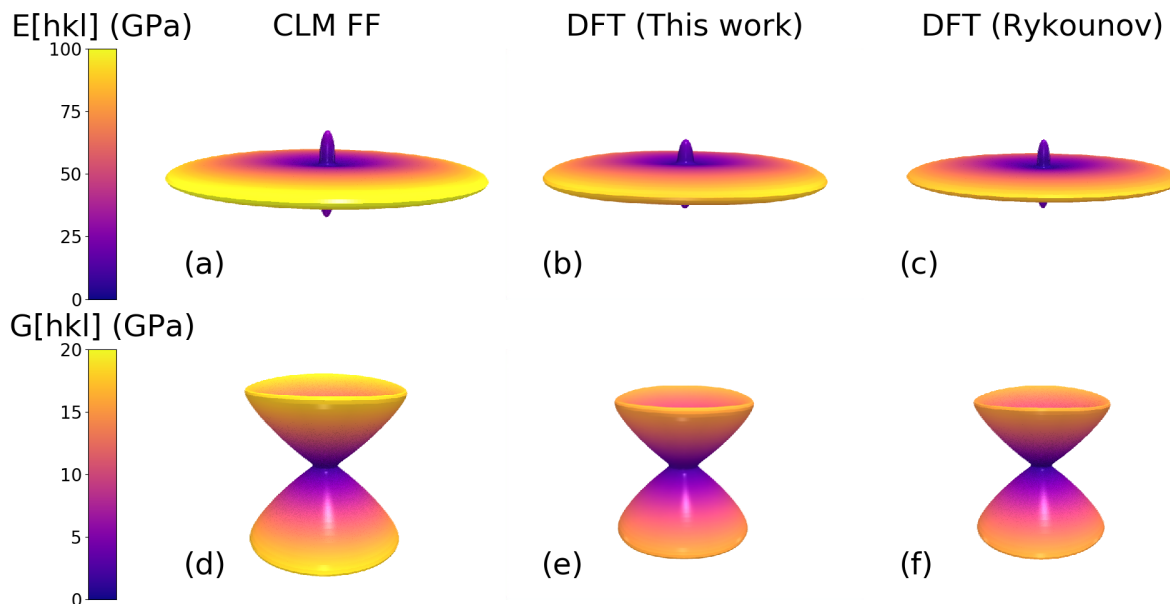


Figure 7: 3D representations of elastic moduli of TATB single crystal derived from the full second-order tensor obtained with the CLM FF (first column), our DFT calculations (middle column), and as reported by Rykounov.³⁷ Young's and shear moduli surfaces at given in the first and second rows, respectively.

sets of DFT calculations are in very good agreement with each other for Young's and shear moduli. The results obtained with the CLM FF are also quite similar to DFT. The main difference is a slightly stiffer overall elasticity, as demonstrated in Table 5. Besides the small differences in amplitude, both shapes are almost identical to the DFT data, indicating very similar elastic anisotropy and directional longitudinal and shear elastic properties.

Intersections between Young's and shear moduli 3D surfaces and the three Cartesian planes (X,Y), (X,Z), (Y,Z) are reported for all DFT calculations (dark lines) and for each FF (colored lines) in Figure 8. Similar to Figure 7, the Young's modulus is given in the first row and the shear modulus is given in the second row. We first note that there is a very good agreement between our DFT calculations (dotted lines) and Rykounov's results (dashed lines), and that these two curves are almost superimposed in every intersection. As can be inferred from Figure 7, the near-isotropic symmetry of TATB single crystal elasticity along directions within the crystal layers in the (X,Y) plane is seen for most of the models except for the shear modulus predicted by the Bedrov FF. The symmetry of the Qin et al.

Young's modulus intersections with the (X,Z) and (Y,Z) planes is distinctly less anisotropic (i.e., more circular) compared to the other models. Unlike for all the other models, the shear surface of Qin et al. exhibits very different symmetry for intersections with the (X,Z) and (Y,Z) planes and these intersections are also distinctly less anisotropic.

Focusing on the FF results, one can see that both ReaxFF-2018 and ReaxFF-LG predict intersection shapes that are consistent with Rykounov and our DFT predictions, but with very large stiffnesses (magnitudes). It is clear that ReaxFF-LG does a poor job in accurately predicting the elastic mechanical properties of TATB crystal. The nonreactive FFs generally perform much better compared to the DFT benchmarks. The Bedrov FF consistently underpredicts each intersection, which is consistent with the overly "soft" isotropic averaged responses discussed above. While the Revised Gee FF more closely matches DFT in terms of both amplitude and directional dependence, the best FF candidate for reproducing the DFT data is the CLM FF. Indeed, the CLM FF provides values for the directional Young's and shear moduli that are in very good agreement with both Rykounov and our DFT results. In addition, it exhibits (just as DFT) intersection symmetries that are commensurate with transverse isotropy (i.e., $C_{66} \simeq 0.5[C_{11}C_{12}]$) that is to be expected due to the nearly hexagonal intralayer packing symmetry. These observations lead us to tentatively conclude that the CLM FF is a very good candidate for characterizing the elastic properties of TATB single crystal.

3.4.3 Elasticity at High Pressure

At a pressure of 10 GPa, there is a good agreement between Rykounov and Qin et al. for the elastic moduli but a comparison of the full tensor is not possible. The elastic constants obtained with the Bedrov FF at 10 GPa are quite different and generally lower than the DFT data of Rykounov. For example, the in-plane and out-of-plane stiffness are off by approximately 100 GPa and 30 GPa, respectively. This also propagates to the low values for the different isotropic elastic moduli. The Revised Gee FF and the CLM FF lead to

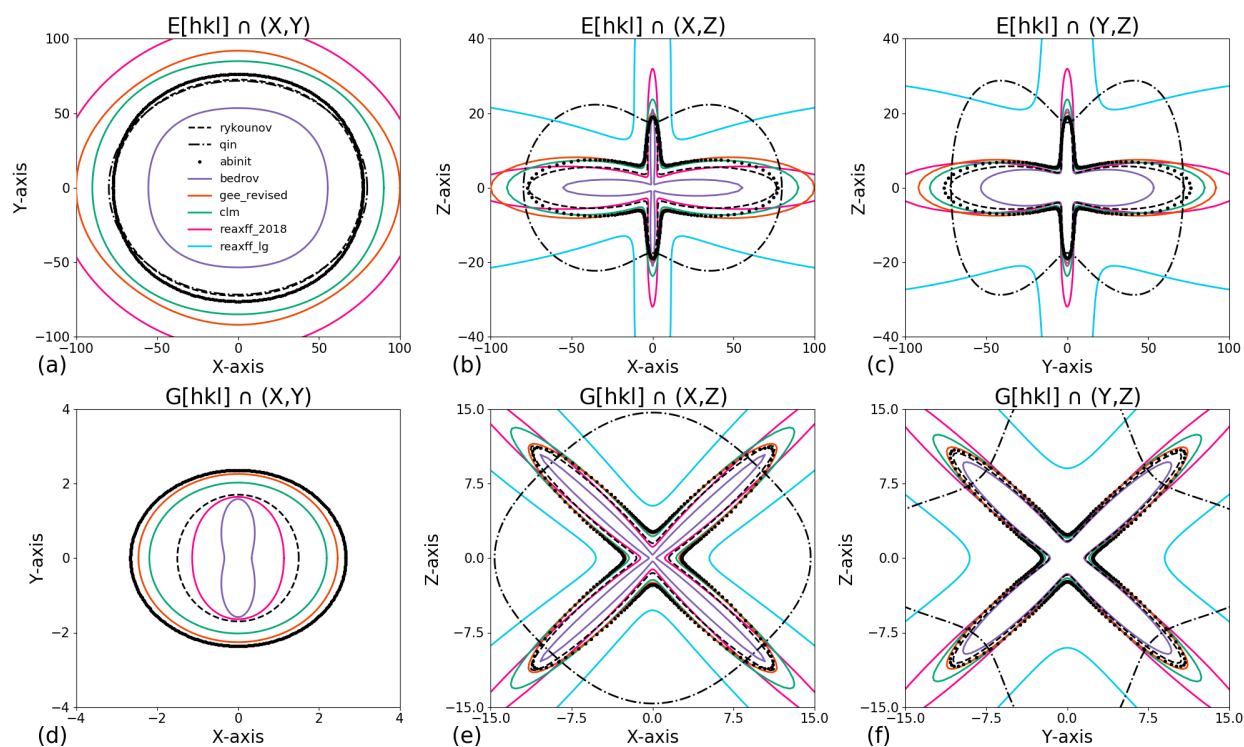


Figure 8: Intersections of the Young's ($E_{[hkl]}$) and shear ($G_{[hkl]}$) moduli surfaces at 0 K and 0 GPa with the (X,Y), (X,Z), and (Y,Z) planes. Predictions from the Bedrov FF, Gee FF (Revised), CLM FF, ReaxFF-2018, and ReaxFF-LG are shown in comparison to the DFT results from Rykounov,³⁷ Qin et al.,³⁸ and our own DFT calculations.

very similar results compared to each other and perform better in reproducing the data from Rykounov in comparison to the other FFs. The biggest differences between these two FFs are the intralayer components C_{11} and C_{22} , for which the CLM FF yields values (≈ 220 GPa) that are lower than the Gee FF values (≈ 265 GPa), with the latter being closer to the DFT data (≈ 255 GPa). As was the case at 0 GPa, one can notice that both ReaxFF-2018 and ReaxFF-LG lead to very large elastic constants and elastic moduli. These FFs lead to a qualitative inaccuracy relative to DFT in that the transverse isotropy symmetry is completely removed, with a factor of ≈ 2 difference between C_{11} and C_{22} . Similar asymmetry is also exhibited through the mismatch between C_{13} and C_{23} elastic constants.

Only the isotropic moduli of Qin et al. are available for comparison at 30 GPa, so little can be said regarding the accuracy of the different FFs. Again, the Bedrov FF is much softer for all three moduli compared to the available DFT data and other FFs, and especially so for

the shear and Young's moduli. All of the C_{ij} are modestly stiffer with the Revised Gee FF compared to the CLM FF. We note that the bulk and shear moduli from Qin et al. are very close to the values obtained with the CLM FF, while values for the Young's modulus differ noticeably. The lack of comprehensive benchmark DFT data at detonation-scale pressures underscores both an ongoing need and potential direction for future work in the development of accurate FF models for TATB that can be applied at its typical operational conditions.

3.5 Layer Sliding

Most inelastic mechanical properties of TATB crystal have only been determined using empirical FFs. To our knowledge, the 2007 study by Zhang⁴¹ and subsequent 2008 work by Zhang et al.⁴² are the only published studies that quantified inelastic deformations in TATB single crystal with electronic structure calculations. The latter study identified a correlation between energy barriers to crystallographic slip and impact sensitivity. Zhang proposed a simplified model for slip involving the glide of a single TATB crystal layer in the unit cell and quantified the 2D energy landscape for translations of that layer using hybrid DFT calculations at the BLYP/DNP level. Plots of the energy landscape and snapshots showing this mechanism are given in Figure 9, panels (a) and (b). Here, the energy for layer sliding

$$E_{\text{slide}}(a_{\text{frac}}, b_{\text{frac}}) = U_{\text{tot}}(a_{\text{frac}}, b_{\text{frac}}) - U_{\text{tot}}^0, \quad (10)$$

is defined relative to a reference structure with potential energy U_{tot}^0 and is computed from a series of single point calculations in which rigid translations of the crystal layers are imposed on that reference structure in the **a-b** plane that yield $U_{\text{tot}}(a_{\text{frac}}, b_{\text{frac}})$. Note that translations along **a** and **b** are given in terms of the unit cell fractional coordinates $a_{\text{frac}}, b_{\text{frac}} \in [0, 1]$. While this layer sliding mechanism is distinct from dislocation glide on the gamma surface for basal slip,^{44,45} it nonetheless provides a useful benchmark for assessing the accuracy of the FFs in capturing processes related to sliding of the basal layers.

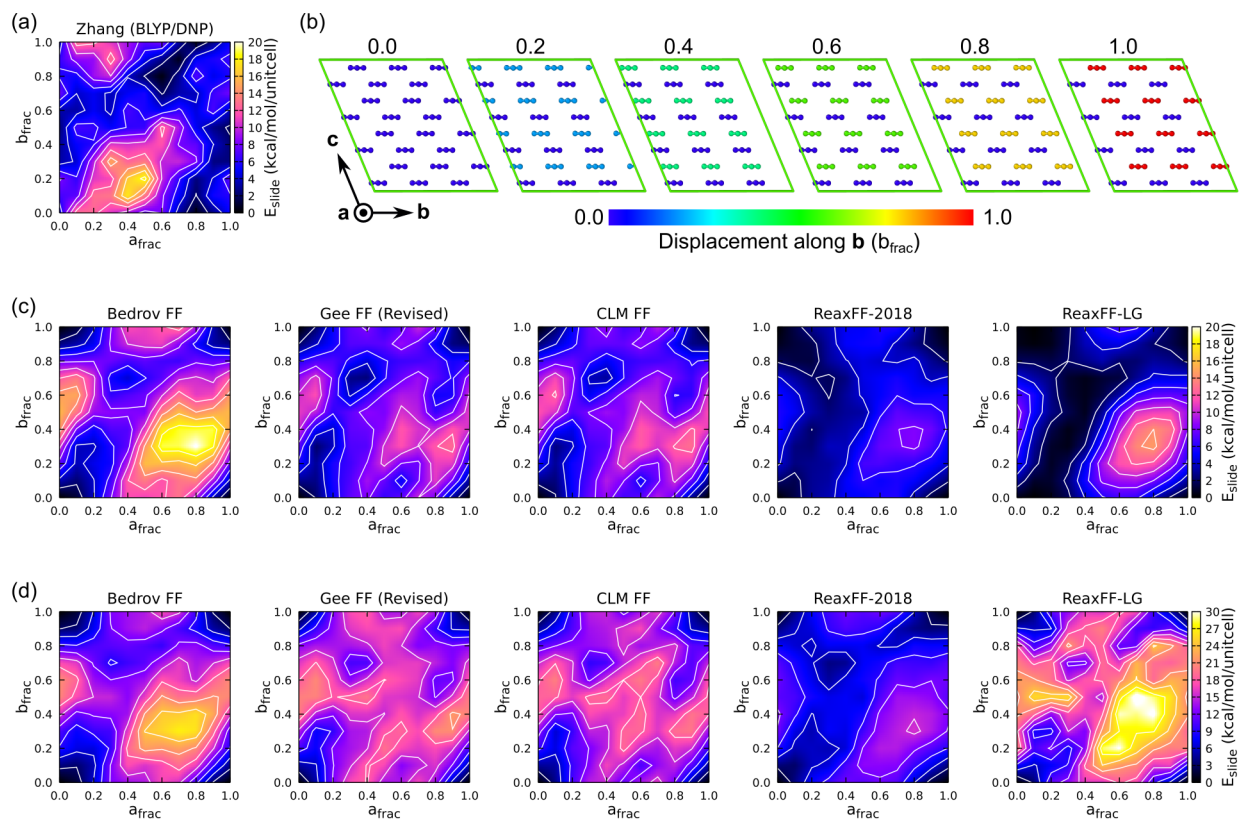


Figure 9: Energy landscape for sliding of TATB crystal layers including (a) the DFT calculations of Zhang⁴¹ and (b) representative snapshots highlighting the layer-sliding mechanism. Analogous FF calculations using initial supercell dimensions determined by (c) Cady and Larson and (d) cell optimization at $P = 1$ atm performed with the respective FF. Contour lines are drawn in $2 \text{ kcal}\cdot\text{mol}^{-1}\cdot\text{unit cell}^{-1}$ increments in panels (a) and (c) and in $3 \text{ kcal}\cdot\text{mol}^{-1}\cdot\text{unit cell}^{-1}$ increments in panel (d).

We considered two series of calculations, both of which were performed using $3\times 3\times 4$ supercells. The first, which corresponds to Figure 9(c), was designed to match Zhang's study as closely as possible. Here, the reference structure (and U_{tot}^0) was obtained by fixing the crystal supercell dimensions based on the Cady and Larson¹ experimental lattice parameters and then performing a geometry optimization of the atomic coordinates. The second approach in panel (d) was similar, but the starting simulation cell parameters were first optimized at 0 K and 1 atm. This second approach compensates for the fact that the various FFs predict equilibrium $d_{(002)}$ spacings that differ from the experimental value. Maximum sliding energy values $E_{\text{slide,max}}$, graphical-based estimates for the maximum barrier to sliding $E_{\text{slide,barrier}}$,

Table 6: TATB crystal layer sliding energies.

Source	$E_{\text{slide,max}}^{\text{Cady\&Larson}}$ (kcal·mol ⁻¹ ·unit cell ⁻¹)	$E_{\text{slide,max}}^{\text{Opt}}$ (kcal·mol ⁻¹ ·unit cell ⁻¹)	$E_{\text{slide,barrier}}^{\text{Cady\&Larson}}$ (kcal·mol ⁻¹ ·unit cell ⁻¹)	$E_{\text{slide,barrier}}^{\text{Opt}}$ (kcal·mol ⁻¹ ·unit cell ⁻¹)	$d_{(002)}^{\text{Opt}}$ (Å)
Zhang ⁴¹	18.62 ^a	-	5 ^c	-	-
Bedrov FF	20.16 (8.3) ^b	26.81	9	13	3.119
Gee FF (Revised)	12.64 (-32.1)	21.67	8	18	3.031
CLM FF	12.76 (-31.5)	20.18	7	16	3.021
ReaxFF-2018	8.35 (-55.2)	15.53	3	7	2.928
ReaxFF-LG	14.51 (-22.0)	31.06	2	19	2.799

^aCady & Larson obtained $d_{(002)} = 3.140$ Å.

^bRelative percent error with respect to Zhang.

^cEstimates for $E_{\text{slide,barrier}}$ obtained from interpolated contour plots with a ± 1 kcal·mol⁻¹·unit cell⁻¹ resolution.

and optimized $d_{(002)}$ spacings are collected in Table 6.

Comparing first the FF results in panel (c) that used the same approach as Zhang, it is clear that the five FFs are qualitatively consistent with each other and with the DFT predictions. In particular, each of the FFs predicts a maximum that lies close to ($a_{\text{frac}} \approx 0.7, b_{\text{frac}} \approx 0.4$). This differs slightly from the DFT result ($a_{\text{frac}} \approx 0.5, b_{\text{frac}} \approx 0.2$). One plausible explanation is that there is a systematic coordinate offset between Zhang’s and our calculations; this is consistent with the fact that Zhang’s data do not exhibit a minimum at ($a_{\text{frac}} = 0.0, b_{\text{frac}} = 0.0$). The Bedrov FF exhibits an $E_{\text{slide,max}}$ that is closest to DFT, but at the same time predicts $E_{\text{slide,barrier}}$ that is substantially higher than DFT. Compared to the Bedrov FF, the other four FFs predict much lower $E_{\text{slide,max}}$ and also smaller $E_{\text{slide,barrier}}$, which is likely due at least in part due to those FFs predicting equilibrium $d_{(002)}$ spacings that are smaller than experiment. Both the Revised Gee FF and the CLM FF predict very similar energy landscape topologies and values for $E_{\text{slide,max}}$ and $E_{\text{slide,barrier}}$, which reflects the subtle differences in the optimized geometries arising from the different intramolecular potential energy functions. Both the CLM FF and ReaxFF-2018 predict sliding barriers that are closest to the DFT baseline. ReaxFF-LG predicts a very small $E_{\text{slide,barrier}}$ that is less than $4k_{\text{B}}T$ at room temperature, indicating that layer sliding with that FF will be quite facile if the Cady and Larson structure is used as a starting configuration.

Additional assessments using optimized simulation cell dimensions in panel (d) shows

that E_{slide} is a strong function of $d_{(002)}$. Topological features of the energy surfaces are generally consistent compared to the results from the Cady and Larson cell geometry, but the absolute values are scaled up by a factor ranging from between 1.3 to 9.5. The most extreme differences occur with ReaxFF-LG, which exhibits $E_{\text{slide,max}}^{\text{Opt}} = 2.1E_{\text{slide,max}}^{\text{Cady\&Larson}}$ and $E_{\text{slide,barrier}}^{\text{Opt}} = 9.5E_{\text{slide,barrier}}^{\text{Cady\&Larson}}$. This is because ReaxFF-LG most significantly underpredicts equilibrium $d_{(002)}$ spacing, differing by more than 10% from the experimental structure.

The Bedrov FF predicts that the nucleation stress for basal glide is orders of magnitude smaller than the nucleation stresses for other deformation mechanisms such as buckling/twinning, transverse dislocations, and shear banding.^{14,46} While one cannot directly compare the above results to previously computed^{44,45} gamma surfaces for basal glide obtained using the Bedrov FF, the similarities above indicate that each FF would likely predict very low barriers to formation of layer sliding defects. As the three nonreactive FFs overpredict the energy barrier to sliding obtained with DFT, previous FF-based predictions^{53,82} for facile basal glide are likely not unreasonable. Such layer sliding has been proposed⁴⁴ as a potential mechanism underlying the unusual second harmonic generation in TATB crystal.^{29,84–86}

4 Conclusions

Insensitive high explosives based on TATB are an indispensable materials class needed for explosives applications where safety is of paramount importance. Despite decades of use and study, the basic material properties of TATB that give rise to its insensitivity are not fully understood. At the same time, MD modeling using empirical FFs has been the only route by which many physical properties of TATB single crystal have been determined at extreme temperatures (>1000 K) and pressures (>10 GPa) typical of “standard” IHE operating conditions. Accurate bottom-up multiscale modeling of TATB at extreme conditions hinges on well-validated MD FFs, but the generic and special-purpose FFs used in MD simulations of

TATB have not been comprehensively tested and in some instances have known deficiencies. To this end, we collected a comprehensive set of (quasi)static TATB physical properties that were determined through experiments and electronic structure theory and applied this data set to validate four widely used TATB FFs and a new TATB FF developed here.

Benchmark data for validation testing included a wide variety of experimental measurements, including vibrational spectra, the TATB crystal temperature-pressure-dependent equation of state and lattice parameters, thermodynamics of phase transitions to the gaseous and liquids states, and the pressure-dependent lattice parameters of a confirmed TATB crystal polymorph. Important data needed for accurate modeling of TATB crystal mechanics could only be sourced from electronic structure theory studies, which included dimer energy landscapes, the pressure-dependent elastic tensor, and the energy landscape for inelastic deformation via sliding of TATB crystal layers. Established FFs considered in this work include variants of the nonreactive models originally developed by Gee et al.¹⁰ and Bedrov et al.¹¹ as well as two reactive models based on the ReaxFF formalism, including ReaxFF-LG¹² and ReaxFF-2018.¹³ We also developed and tested a new nonreactive FF, which we denote as the CEA-LLNL-Missouri FF (or CLM FF).

As a general assessment, we found that the existing nonreactive FFs by Gee and Bedrov were more accurate than either ReaxFF variant in describing the physical properties of TATB. The ReaxFF-LG variant in particular deviated most significantly out of any FF across essentially the entire validation test set, and in some cases those deviations were substantial and on the order of 100-500%. Our new CLM FF was found to consistently yield similar or better agreement with experiment and electronic structure theory than any of the existing FF models, and presents a distinct improvement in accurately modeling this material under detonation-scale pressures (30+ GPa).

The results of this study underscore both a need for more comprehensive high-temperature and high-pressure experimental measurements of TATB single-crystal physical properties and for validation testing of MD FFs used to model TATB. Such testing is necessary for improving

the accuracy of FF-based assessments of complicated dynamic material properties that are exceedingly difficult to measure in experiments such as (anisotropic) transport coefficients, single-crystal strength, and shock responses above the Hugoniot elastic limit to include details of hot spot formation and chemical initiation. Detailed assessments of existing TATB FFs presented here are expected to help guide interpretation of past MD studies, inform future choices for application-oriented MD studies on TATB crystal, and provide a road-map for validation testing of new TATB FFs.

Acknowledgement

MPK and LEF thank Rick Gee for useful discussions and assistance with implementing the Gee force field in LAMMPS. This work was performed under the auspices of the U.S. Department of Energy by Lawrence Livermore National Laboratory under Contract DE-AC52-07NA27344. It has been approved for unlimited release under document number LLNL-JRNL-857938-DRAFT. This work was performed under the auspices of an agreement between CEA/DAM and NNSA/DP on cooperation on fundamental science.

References

- (1) Cady, H. H.; Larson, A. C. The crystal structure of 1,3,5-triamino-2,4,6-trinitrobenzene. *Acta Crystallogr.* **18**, 485.
- (2) Dobratz, B. M. The insensitive high explosive triaminotrinitrobenzene (TATB): Development and characterization, 1888 to 1994. 1995; <https://www.osti.gov/biblio/90370>.
- (3) Jackson, C. L.; Wing, J. F. On Tribromotrinitrobenzol. *Am. Chem. J.* **1888**, *10*, 283.
- (4) Östmark, H.; Langlet, A.; Bergman, H.; Wingborg, N.; Wellmar, U.; Bemm, U. FOX-

- 7 - A new explosive with low sensitivity and high performance. 11th Int. Detonation Symposium. 2000.
- (5) Tran, T. D.; Pagoria, P. F.; Hoffman, D. M.; Cunningham, B.; Simpson, R. L.; Lee, R. S.; Cutting, J. L. Small-scale safety and performance characterization of new plastic bonded explosives containing LLM-105. 12th Int. Detonation Symposium. 2002.
- (6) Maienschein, J. L. Research topics in explosives - a look at explosives behaviors. *J. Phys.: Conf. Ser.* **2014**, *500*, 052027.
- (7) Wang, Y.; Liu, Y.; Song, S.; Yang, Z.; Qi, X.; Wang, K.; Liu, Y.; Zhang, Q.; Tian, Y. Accelerating the discovery of insensitive high-energy-density materials by a materials genome approach. *Nature Commun.* **2018**, *9*, 2444.
- (8) Tarver, C. M.; Kury, J. W.; Breithaupt, R. D. Detonation waves in triaminotrinitrobenzene. *J. Appl. Phys.* **1997**, *82*, 3771–3782.
- (9) Bassett, W. P.; Johnson, B. P.; Salvati III, L.; Nissen, E. J.; Bhowmick, M.; Dlott, D. D. Shock initiation microscopy with high time and space resolution. *Propellants Explos. Pyrotech.* **2020**, *45*, 223–235.
- (10) Gee, R. H.; Roszak, S.; Balasubramanian, K.; Fried, L. E. Ab initio based force field and molecular dynamics simulations of crystalline TATB. *J. Chem. Phys.* **2004**, *120*, 7059.
- (11) Bedrov, D.; Borodin, O.; Smith, G. D.; Sewell, T. D.; Dattelbaum, D. M.; Stevens, L. L. A molecular dynamics simulation study of crystalline 1,3,5-triamino-2,4,6-trinitrobenzene as a function of pressure and temperature. *J. Chem. Phys.* **2009**, *131*, 224703.
- (12) Liu, L.; Liu, Y.; Zybin, S. V.; Sun, H.; Goddard, W. A. I. ReaxFF-1g: Correction of the

- ReaxFF reactive force field for London dispersion, with applications to the equations of state for energetic materials. *J. Phys. Chem. A* **2011**, *115*, 11016–11022.
- (13) Wood, M. A.; Kittell, D. E.; Yarrington, C. D.; Thompson, A. P. Multiscale modeling of shock wave localization in porous energetic material. *Phys. Rev. B* **2018**, *97*, 014109.
- (14) Kroonblawd, M. P.; Steele, B. A.; Nelms, M. D.; Fried, L. E.; Austin, R. A. Anisotropic Strength Behavior of Single-Crystal TATB. *Model. Simul. Mater. Sci. Eng.* **2022**, *30*, 014004.
- (15) Lafourcade, P.; Maillet, J.-B.; Bruzy, N.; Denoual, C. Elastic anisotropy of 1,3,5-triamino-2,4,6-trinitrobenzene as a function of temperature and pressure: A molecular dynamics study. *Propellants Explos. Pyrotech.* **2022**, *47*, e202100384.
- (16) Plisson, T.; Pineau, N.; Weck, G.; Bruneton, E.; Guignot, N.; Loubeyre, P. Equation of state of 1,3,5-triamino-2,4,6-trinitrobenzene up to 66 GPa. *J. Appl. Phys.* **2017**, *122*, 235901.
- (17) Stevens, L. L.; Velisavljevic, N.; Hooks, D. E.; Dattelbaum, D. M. Hydrostatic Compression Curve for Triamino-Trinitrobenzene Determined to 13.0 ÅGPa with Powder X-Ray Diffraction. *Propellants Explos. Pyrotech.* *33*, 286.
- (18) Kolb, J. R.; Rizzo, H. F. Growth of 1,3,5-Triamino-2,4,6-trinitrobenzene (TATB) I. Anisotropic thermal expansion. *Propellants Explos. Pyrotech.* **1979**, *4*, 10–16.
- (19) Sun, J.; Kang, B.; Xue, C.; Liu, Y.; Xia, Y.; Liu, X.; Zhang, W. Crystal state of 1,3,5-triamino-2,4,6-trinitrobenzene (tatb) undergoing thermal cycling process. *J. Energ. Mat.* **2010**, *28*, 189–201.
- (20) Marshall, M. C.; Fernandez-Panella, A.; Myers, T. W.; Eggert, J. H.; Erskine, D. J.; Bastea, S.; Fried, L. E.; Leininger, L. D. Shock Hugoniot measurements of single-crystal

- 1,3,5-triamino-2,4,6-trinitrobenzene (TATB) compressed to 83 GPa. *J. Appl. Phys.* **2020**, *127*, 185901.
- (21) Taw, M. R.; Yeager, J. D.; Hooks, D. E.; Carvajal, T. M.; Bahr, D. F. The mechanical properties of as-grown noncubic organic molecular crystals assessed by nanoindentation. *J. Mater. Res.* **2017**, *32*, 2728.
- (22) Mathew, N.; Sewell, T. D. Nanoindentation of the Triclinic Molecular Crystal 1,3,5-Triamino-2,4,6-trinitrobenzene: A Molecular Dynamics Study. *J. Phys. Chem. C* **2016**, *120*, 8266.
- (23) Zhakhovsky, V. V.; Budzevich, M. M.; Inogamov, N. A.; Oleynik, I. I.; White, C. T. Two-Zone Elastic-Plastic Single Shock Waves in Solids. *Phys. Rev. Lett.* **2011**, *107*, 135502.
- (24) Kroonblawd, M. P.; Sewell, T. D.; Maillet, J.-B. Characteristics of energy exchange between inter- and intramolecular degrees of freedom in crystalline 1,3,5-triamino-2,4,6-trinitrobenzene (TATB) with implications for coarse-grained simulations of shock waves in polyatomic molecular crystals. *J. Chem. Phys.* **2016**, *144*, 064501.
- (25) Zepeda-Ruiz, L. A.; Stukowski, A.; Oettel, T.; Bulatov, V. V. Probing the limits of metal plasticity with molecular dynamics simulations. *Nature* **2017**, *550*, 492.
- (26) Rosen, J. M.; Dickinson, C. Vapor pressures and heats of sublimation of some high-melting organic explosives. *J. Chem. Eng. Data* **1969**, *14*, 120–124.
- (27) Garza, R. G. Thermogravimetric Study of TATB and Two TATB-Based Explosives. 1979.
- (28) Stolovy, A.; Jones, J., E. C.; Aviles, J., J. B.; Namenson, A. I.; Fraser, W. A. Exothermic reactions in TATB initiated by an electron beam. *J. Chem. Phys.* **1983**, *78*, 229–235.

- (29) Bowlan, P.; Suvorova, N.; Remelius, D.; Smilowitz, L.; Henson, B. F. Tracking thermal decomposition chemistry in secondary solid explosives with x-ray diffraction. *J. Phys. Chem. A* **2022**, *126*, 4497–4506.
- (30) Filippini, G.; Gavezzotti, A. The crystal structure of 1,3,5-triamino-2,4,6-trinitrobenzene: Centrosymmetric or non-centrosymmetric? *Chem. Phys. Lett.* **1994**, *231*, 86–92.
- (31) Steele, B. A.; Clarke, S. M.; Kroonblawd, M. P.; Kuo, I.-F. W.; Pagoria, P. F.; Tkachev, S. N.; Smith, J. S.; Bastea, S.; Fried, L. E.; Zaug, J. M. et al. Pressure-induced phase transition in 1,3,5-triamino-2,4,6-trinitrobenzene (TATB). *Appl. Phys. Lett.* **2019**, *114*, 191901.
- (32) Satija, S. K.; Swanson, B.; Eckert, J.; Goldstone, J. A. High-pressure Raman scattering and inelastic neutron scattering studies of triaminotrinitrobenzene. *J. Phys. Chem.* **1991**, *95*, 10103–10109.
- (33) McGrane, S. D.; Shreve, A. P. Temperature-dependent Raman spectra of triaminotrinitrobenzene: Anharmonic mode couplings in an energetic material. *J. Chem. Phys.* **2003**, *119*, 5834–5841.
- (34) McGrane, S. D.; Barber, J.; Quenneville, J. Anharmonic Vibrational Properties of Explosives from Temperature-Dependent Raman. *J. Phys. Chem. A* **2005**, *109*, 9919–9927.
- (35) Pravica, M.; Yulga, B.; Liu, Z.; Tschauner, O. Infrared study of 1,3,5-triamino-2,4,6-trinitrobenzene under high pressure. *Phys. Rev. B* **2007**, *76*, 064102.
- (36) Valenzano, L.; Slough, W. J.; Perger, W. Accurate prediction of second-order elastic constants from first principles: PETN and TATB. *AIP Conf. Proc.* **2012**, *1426*, 1191–1194.

- (37) Rykounov, A. A. Investigation of the pressure dependent thermodynamic and elastic properties of 1,3,5-triamino-2,4,6-trinitrobenzene using dispersion corrected density functional theory. *J. Appl. Phys.* **2015**, *117*, 215901.
- (38) Qin, H.; Yan, B.-L.; Zhong, M.; Jiang, C.-L.; Liu, F.-S.; Tang, B.; Liu, Q.-J. First-principles study of structural, elastic, and electronic properties of triclinic TATB under different pressures. *Phys. B: Condens. Matter* **2019**, *552*, 151–158.
- (39) Long, Y.; Chen, J. Theoretical study of the phonon–phonon scattering mechanism and the thermal conductive coefficients for energetic material. *Phil. Mag.* **2017**, *97*, 2575.
- (40) Taylor, D. E. Intermolecular forces and molecular dynamics simulation of 1,3,5-triamino-2,4,6-trinitrobenzene (tatb) using symmetry adapted perturbation theory. *J. Phys. Chem. A* **2013**, *117*, 3507–3520.
- (41) Zhang, C. Investigation of the Slide of the Single Layer of the 1,3,5-Triamino-2,4,6-trinitrobenzene Crystal: A Sliding Potential and Orientation. *J. Phys. Chem. B* **2007**, *111*, 14295–14298.
- (42) Zhang, C.; Wang, X.; Huang, H. π -Stacked Interactions in Explosive Crystals: Buffers against External Mechanical Stimuli. *J. Am. Chem. Soc.* **2008**, *130*, 8359–8365.
- (43) Fan, H.; Long, Y.; Ding, L.; Chen, J.; Nie, F.-D. A theoretical study of elastic anisotropy and thermal conductivity for TATB under pressure. *Comp. Mat. Sci.* **2017**, *131*, 321.
- (44) Mathew, N.; Sewell, T. D. Generalized stacking fault energies in the basal plane of triclinic molecular crystal 1,3,5-triamino-2,4,6-trinitrobenzene (TATB). *Phil. Mag.* **2015**, *95*, 424.
- (45) Lafourcade, P.; Denoual, C.; Maillet, J.-B. Dislocation core structure at finite tempera-

- ture inferred by molecular dynamics simulations for 1,3,5-triamino-2,4,6-trinitrobenzene single crystal. *J. Phys. Chem. C* **2017**, *121*, 7442.
- (46) Lafourcade, P.; Denoual, C.; Maillet, J.-B. Irreversible deformation mechanisms for 1,3,5-triamino-2,4,6-trinitrobenzene single crystal through molecular dynamics simulations. *J. Phys. Chem. C* **2018**, *122*, 14954.
- (47) Lafourcade, P.; Denoual, C.; Maillet, J.-B. Mesoscopic constitutive law with nonlinear elasticity and phase transformation for the twinning-buckling of TATB under dynamic loading. *Phys. Rev. Mat.* **2019**, *3*, 053610.
- (48) Kroonblawd, M. P.; Fried, L. E. High explosive ignition through chemically activated nanoscale shear bands. *Phys. Rev. Lett.* **2020**, *124*, 206002.
- (49) Zhao, P.; Kroonblawd, M. P.; Mathew, N.; Sewell, T. Strongly anisotropic thermomechanical response to shock wave loading in oriented samples of the triclinic molecular crystal 1,3,5-triamino-2,4,6-trinitrobenzene. *J. Phys. Chem. C* **2021**, *125*, 22747–22765.
- (50) Mathew, N.; Sewell, T. D.; Thompson, D. L. Anisotropy in surface-initiated melting of the triclinic molecular crystal 1,3,5-triamino-2,4,6-trinitrobenzene: A molecular dynamics study. *J. Chem. Phys.* **2015**, *143*, 094706.
- (51) Mathew, N.; Kroonblawd, M. P.; Sewell, T.; Thompson, D. L. Predicted melt curve and liquid-state transport properties of TATB from molecular dynamics simulations. *Mol. Sim.* **2018**, *44*, 613–622.
- (52) Kroonblawd, M. P.; Sewell, T. D. Theoretical determination of anisotropic thermal conductivity for crystalline 1,3,5-triamino-2,4,6-trinitrobenzene (TATB). *J. Chem. Phys.* **2013**, *139*, 074503.
- (53) Kroonblawd, M. P.; Sewell, T. D. Theoretical determination of anisotropic thermal

- conductivity for initially defect-free and defective TATB single crystals. *J. Chem. Phys.* **2014**, *141*, 184501.
- (54) Kroonblawd, M. P.; Sewell, T. D. Predicted anisotropic thermal conductivity for crystalline 1,3,5-triamino-2,4,6-trinitrobenzene (TATB): Temperature and pressure dependence and sensitivity to intramolecular force field terms. *Propellants Explos. Pyrotech.* *41*, 502.
- (55) Zhao, P.; Lee, S.; Sewell, T.; Udaykumar, H. S. Tandem molecular dynamics and continuum studies of shock-induced pore collapse in TATB. *Propellants Explos. Pyrotech.* *45*, 196.
- (56) Hamilton, B. W.; Kroonblawd, M. P.; Li, C.; Strachan, A. A hotspot's better half: Non-equilibrium intra-molecular strain in shock physics. *J. Phys. Chem. Lett.* **2021**, *12*, 2756.
- (57) Hamilton, B. W.; Kroonblawd, M. P.; Strachan, A. The potential energy hotspot: Effects of impact velocity, defect geometry, and crystallographic orientation. *J. Phys. Chem. C* **2022**, *126*, 3743–3755.
- (58) Hamilton, B. W.; Germann, T. C. Energy localization efficiency in 1,3,5-trinitro-2,4,6-triaminobenzene pore collapse mechanisms. *J. Appl. Phys.* **2023**, *133*, 035901.
- (59) Kroonblawd, M. P.; Sewell, T. D. Anisotropic relaxation of idealized hot spots in crystalline 1,3,5-triamino-2,4,6-trinitrobenzene (TATB). *J. Phys. Chem. C* **2016**, *120*, 17214.
- (60) Kroonblawd, M. P.; Hamilton, B. W.; Strachan, A. Fourier-like Thermal Relaxation of Nanoscale Explosive Hot Spots. *J. Phys. Chem. C* **2021**, *125*, 20570–20582.
- (61) Menikoff, R.; Sewell, T. D. Constituent properties of HMX needed for mesoscale simulations. *Combust. Theory Model.* **2002**, *6*, 103.

- (62) Thompson, A. P.; Aktulga, H. M.; Berger, R.; Bolintineanu, D. S.; Brown, W. M.; Crozier, P. S.; in 't Veld, P. J.; Kohlmeyer, A.; Moore, S. G.; Nguyen, T. D. et al. LAMMPS - a flexible simulation tool for particle-based materials modeling at the atomic, meso, and continuum scales. *Comp. Phys. Comm.* **2022**, *271*, 108171, LAMMPS is available at <http://lammmps.sandia.gov>.
- (63) Shinoda, W.; Shiga, M.; Mikami, M. Rapid estimation of elastic constants by molecular dynamics simulation under constant stress. *Phys. Rev. B* **2004**, *69*, 134103.
- (64) Tuckerman, M. E.; Alejandre, J.; LÃşpez-RendÃşn, R.; Jochim, A. L.; Martyna, G. J. A Liouville-operator derived measure-preserving integrator for molecular dynamics simulations in the isothermalÃşisobaric ensemble. *J. Phys. A: Math. Gen.* **2006**, *39*, 5629.
- (65) Wolf, D.; Keblinski, P.; Phillpot, S. R.; Eggebrecht, J. Exact method for the simulation of Coulombic systems by spherically truncated, pairwise rÃş¹ summation. *J. Chem. Phys.* **1999**, *110*, 8254.
- (66) Rai, N.; Bhatt, D.; Siepmann, J. I.; Fried, L. E. Monte Carlo simulations of 1,3,5-triamino-2,4,6-trinitrobenzene (TATB): Pressure and temperature effects for the solid phase and vapor-liquid phase equilibria. *J. Chem. Phys.* **2008**, *129*, 194510.
- (67) Waldman, M.; Hagler, A. New combining rules for rare gas van der waals parameters. *J. Comp. Chem.* **1993**, *14*, 1077–1084.
- (68) Liu, H.; Zhao, J.; Ji, G.; Wei, D.; Gong, Z. Vibrational properties of molecule and crystal of TATB: A comparative density functional study. *Phys. Lett. A* **2006**, *358*, 63–69.
- (69) Mayo, S. L.; Olafson, B. D.; Goddard, W. A. DREIDING: a generic force field for molecular simulations. *J. Phys. Chem.* **1990**, *94*, 8897–8909.

- (70) Manaa, M. R.; Gee, R. H.; Fried, L. E. Internal rotation of amino and nitro groups in TATB: AĀŁ MP2 versus DFT (B3LYP). *J. Phys. Chem. A* **2002**, *106*, 8806–8810.
- (71) Wen, Y.; Xue, X.; Long, X.; Zhang, C. Cluster Evolution at Early Stages of 1,3,5-Triamino-2,4,6-trinitrobenzene under Various Heating Conditions: A Molecular Reactive Force Field Study. *J. Phys. Chem. A* **2016**, *120*, 3929–3937.
- (72) Tiwari, S. C.; Nomura, K.-i.; Kalia, R. K.; Nakano, A.; Vashishta, P. Multiple Reaction Pathways in Shocked 2,4,6-Triamino-1,3,5-trinitrobenzene Crystal. *J. Phys. Chem. C* **2017**, *121*, 16029–16034.
- (73) Bidault, X.; Pineau, N. Impact of surface energy on the shock properties of granular explosives. *J. Chem. Phys.* **2018**, *148*, 034704.
- (74) Hamilton, B. W.; Kroonblawd, M. P.; Islam, M. M.; Strachan, A. Sensitivity of the Shock Initiation Threshold of 1,3,5-Triamino-2,4,6-trinitrobenzene (TATB) to Nuclear Quantum Effects. *J. Phys. Chem. C* **2019**, *123*, 21969–21981.
- (75) Hamilton, B. W.; Kroonblawd, M. P.; Strachan, A. Extemporaneous Mechanochemistry: Shock-Wave-Induced Ultrafast Chemical Reactions Due to Intramolecular Strain Energy. *J. Phys. Chem. Lett.* **2022**, *13*, 6657–6663.
- (76) Kober, E. M. Developing Reaction Chemistry Models from Reactive Molecular Dynamics: TATB. *Propellants Explos. Pyrotech.* **2022**, *47*, e202100386.
- (77) Lafourcade, P.; Maillet, J.-B.; Roche, J.; Sakano, M.; Hamilton, B. W.; Strachan, A. Multiscale Reactive Model for 1,3,5-Triamino-2,4,6-trinitrobenzene Inferred by Reactive MD Simulations and Unsupervised Learning. *J. Phys. Chem. C* **2023**, *127*, 15556–15572.
- (78) Rappe, A. K.; Goddard, W. A. I. Charge equilibration for molecular dynamics simulations. *J. Phys. Chem.* **1991**, *95*, 3358–3363.

- (79) Brehm, M.; Kirchner, B. TRAVIS - A free analyzer and visualizer for Monte Carlo and molecular dynamics trajectories. *J. Chem. Inf. Model.* **2011**, *51*, 2007–2023.
- (80) Michalchuk, A. A. L.; Hemingway, J.; Morrison, C. A. Predicting the impact sensitivities of energetic materials through zone-center phonon up-pumping. *J. Chem. Phys.* **2021**, *154*, 064105.
- (81) Liu, Z.; Chung, P. W. Unusual thermal transport in molecular crystals. *Mater. Today Phys.* **2023**, *36*, 101163.
- (82) Steele, B. A.; Stavrou, E.; Prakapenka, V. B.; Kroonblawd, M. P.; Kuo, I.-F. W. High-pressure equation of state of 1,3,5-triamino-2,4,6-trinitrobenzene: Insights into the monoclinic phase transition, hydrogen bonding, and anharmonicity. *J. Phys. Chem. A* **2020**, *124*, 10580.
- (83) Willey, T. M.; vanBuuren, T.; Lee, J. R.; Overturf, G. E.; Kinney, J. H.; Handly, J.; Weeks, B. L.; Ilavsky, J. Changes in Pore Size Distribution upon Thermal Cycling of TATB-based Explosives Measured by Ultra-Small Angle X-Ray Scattering. *Propellants Explos. Pyrotech.* *31*, 466.
- (84) Ledoux, I.; Zyss, J.; Siegel, J.; Brienne, J.; Lehn, J.-M. Reprint of: Second-harmonic generation from non-dipolar non-centrosymmetric aromatic charge-transfer molecules. *Chem. Phys. Lett.* **2013**, *589*, 47–50.
- (85) Voigt-Martin, I. G.; Li, G.; Yakimanski, A. A.; Wolff, J. J.; Gross, H. Use of Electron Diffraction and High-Resolution Imaging To Explain Why the Non-dipolar 1,3,5-Triamino-2,4,6-trinitrobenzene Displays Strong Powder Second Harmonic Generation Efficiency. *J. Phys. Chem. A* **1997**, *101*, 7265–7276.
- (86) Son, S. F.; Asay, B. W.; Henson, B. F.; Sander, R. K.; Ali, A. N.; Zielinski, P. M.; Phillips, D. S.; Schwarz, R. B.; Skidmore, C. B. Dynamic Observation of a Thermally

- Activated Structure Change in 1,3,5-Triamino-2,4,6-trinitrobenzene (TATB) by Second Harmonic Generation. *J. Phys. Chem. B* **1999**, *103*, 5434–5440.
- (87) Kroonblawd, M. P.; Austin, R. A. Sensitivity of pore collapse heating to the melting temperature and shear viscosity of hmx. *Mech. Mat.* **2021**, *152*, 103644.
- (88) Kroonblawd, M. P.; Springer, H. K. Predicted melt curve and liquid shear viscosity of rdx up to 30 ÅGPa. *Propellants Explos. Pyrotech.* **2022**, *47*, e202100328.
- (89) Tow, G. M.; Larentzos, J. P.; Sellers, M. S.; LÅnsal, M.; Brennan, J. K. Predicting melt curves of energetic materials using molecular models. *Propellants Explos. Pyrotech.* **2022**, *47*, e202100363.
- (90) Perdew, J. P.; Burke, K.; Ernzerhof, M. Generalized Gradient Approximation Made Simple. *Phys. Rev. Lett.* **1996**, *77*, 3865–3868.
- (91) Grimme, S. Semiempirical GGA-type density functional constructed with a long-range dispersion correction. *J. Comp. Chem.* *27*, 1787.
- (92) Blöchl, P. E. Projector augmented-wave method. *Phys. Rev. B* **1994**, *50*, 17953–17979.
- (93) Gonze, X.; Jollet, F.; Abreu Araujo, F.; Adams, D.; Amadon, B.; Applencourt, T.; Audouze, C.; Beuken, J.-M.; Bieder, J.; Bokhanchuk, A. et al. Recent developments in the ABINIT software package. *Comput. Phys. Commun.* **2016**, *205*, 106–131.
- (94) Ranganathan, S. I.; Ostoja-Starzewski, M. Universal Elastic Anisotropy Index. *Phys. Rev. Lett.* **2008**, *101*, 055504.

Graphical TOC Entry

